

1 **Detection and geometric characterization of rock mass**
2 **discontinuities using a 3D high-resolution digital outcrop**
3 **model generated from RPAS imagery - Ormea rock slope,**
4 **Italy**

5
6 Niccolò Menegoni¹, Daniele Giordan², Cesare Perotti¹, Dwayne D. Tannant²

7
8 1 University of Pavia, Pavia, Italy

9 2 National Research Council of Italy, Research Institute for Geo-Hydrological Protection
10 (CNR-IRPI), Torino, Italy

11 3 University of British Columbia, Kelowna, Canada

12
13 Corresponding Author: daniele.giordan@irpi.cnr.it
14
15

16 **Abstract**

17 The use of a remotely piloted aircraft system (RPAS) and digital photogrammetry is valuable
18 for the detection of discontinuities in areas where field mapping and terrestrial photogrammetry
19 or laser scanner surveys cannot be employed because the slope is unsafe, inaccessible, or
20 characterized by a complex geometry with areas not visible from the ground. Using the
21 Structure-from-Motion method, the acquired images can be used to create a 3D texturized
22 digital outcrop model (TDOM) and a detailed point cloud representing the rock outcrop.
23 Discontinuity orientations in a complex rock outcrop in Italy were mapped in the field using a
24 geological compass and by manual and automated techniques using a TDOM and point cloud
25 generated from RPAS imagery. There was a good agreement between the field measurements
26 and manual mapping in the TDOM. Semi-automated discontinuity mapping using the point
27 cloud was performed using the DSE, qFacet FM, and qFacet KD-tree methods applied to the
28 same 3D model. Significant discrepancies were found between the semi-automatic and manual
29 methods. In particular, the automatic methods did not adequately detect discontinuities that are
30 perpendicular to the slope face (bedding planes in the case study). These differences in
31 detection of discontinuities can adversely influence the kinematic analysis of potential rock
32 slope failure mechanisms. We use the case study to demonstrate a workflow that can be
33 considered a powerful approach to accurately map discontinuities with results comparable to
34 field measurements. The combined use of TDOM and RPAS dramatically increases the
35 discontinuity data because RPAS is able to supply a good coverage of inaccessible or hidden

36 portions of the slope and TDOM is a powerful representation of the reality that can be used to
37 map discontinuity orientations including those that are oriented perpendicular to the slope.

38

39 **Keywords**

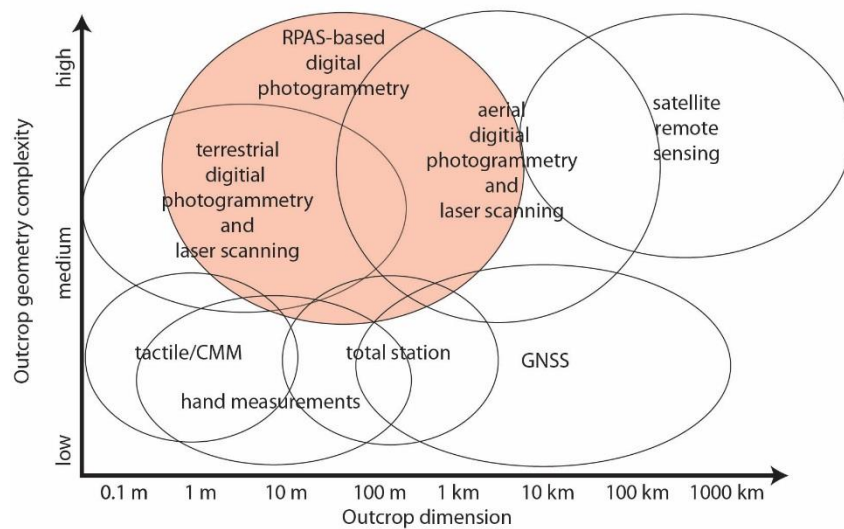
40 Remotely Piloted Aerial Systems, rock slope instabilities, textured digital outcrop models,
41 discontinuity mapping, semi-automatic discontinuity identification

42 **1 Introduction**

43 Detection and mapping of rock discontinuities are important not only for geological studies
44 (structural geology, rock mechanics, etc.), but also for engineering and industrial applications
45 (e.g., slope stability, tunneling, quarry activity, CO₂ and nuclear waste storage, oil and gas
46 exploitation). Therefore, the acquisition of accurate quantitative discontinuity data, which are
47 not affected by biases and censoring is very important. A recent tool that can be useful for this
48 purpose is a Digital Outcrop Model (DOM) (Powers et al., 1996).

49 In the past twenty years, the applications in geosciences of remote sensing investigations for
50 the construction of DOM have rapidly improved (e.g. Powers et al., 1996; Xu et al., 2000;
51 Pringle et al., 2004; Bellian et al., 2005; Sturzenegger and Stead, 2009; Jaboyedoff et al., 2012;
52 Westoby et al., 2012; Humair et al., 2013; Bemis et al., 2014; Spreafico et al., 2016; Tavani et
53 al., 2016). The most common techniques used to generate highly detailed DOMs are terrestrial
54 laser scanning and digital photogrammetry. While laser scanning can be very expensive and
55 requires complex survey planning (heavy and bulky equipment), digital photogrammetry
56 allows for acquisition of high-resolution data with a lower cost and with more user-friendly
57 survey planning (Remondino and El-Hakim, 2006; Westoby et al., 2012). Developments in
58 RGB cameras and Remotely Piloted Aircraft Systems (RPAS) (Colomina and Molina, 2014)
59 have increased the applications of RPAS-based Digital Photogrammetry (RPAS-DP) in
60 geosciences (e.g. Niethammer et al., 2012; Westoby et al., 2012; ; Lucieer et al., 2013; Bemis
61 et al., 2014; Tannant 2015; Casella et al., 2016; Salvini et al., 2016; Chesley et al., 2017; Török
62 et al., 2017). RPAS-DP can be used in a wide variety of scenarios (Nex and Remondino, 2014;
63 Fig. 1), from meter scale (e.g. Cawood et al., 2017; Tannant et al., 2017) to kilometer scale

64 (e.g. Gonçalves and Henriques, 2015) and from simple geometries (e.g. Chesley et al., 2017)
 65 to complex geometries (e.g. Cawood et al., 2017). Moreover, RPAS-DP can also overcome the
 66 occlusion effects that often affect terrestrial photogrammetry and laser scanning techniques
 67 because the RPAS platform can remotely move the camera to more optimum user-inaccessible
 68 positions. The use of different points of view is important for the reduction of occlusions or
 69 areas that cannot be measured using terrestrial technologies that are restricted to data collection
 70 from the ground.



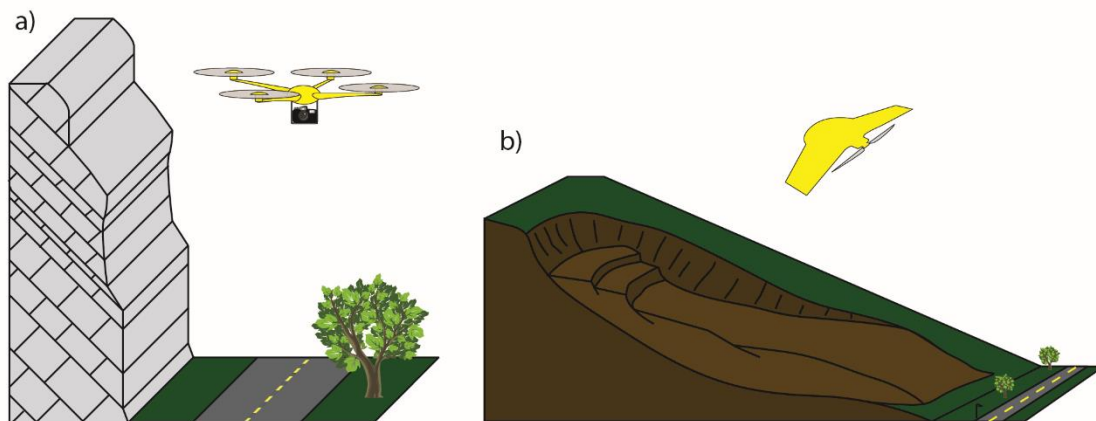
71
 72 Fig. 1. Applicability of different mapping techniques in relation to the outcrop dimensions
 73 and geometry complexity (modified after Nex and Remondino, 2014).

74 Due to the presence of a GNSS/INS system on an RPAS platform, it is possible to measure the
 75 camera location for each image that is taken. This then allows for direct georeferencing of
 76 photogrammetric products produced using Structure-from-Motion (SfM) digital processing of
 77 the images (Nex and Remondino, 2014).

78 The principal products from SfM-based image processing are: (i) Point Cloud (PC), (ii) Digital
 79 Surface Model (DSM), (iii) orthoimage, and (iv) 3D texturized model. In geoscience, the latter
 80 product is also called Texturized Digital Outcrop Model (TDOM). The resolution of these SfM-
 81 based photogrammetric products depends directly on the resolution of the camera sensor
 82 (number of pixels and pixel size), the camera lens (focal length) and the distance between the
 83 camera and the object. The accuracy depends on the quality of the camera and RPAS
 84 components (e.g. camera shutter, internal and external camera stabilizer, GNSS/IMU system),
 85 the RPAS-DP survey planning (e.g. image overlap, weather and lighting conditions, presence

86 or absence of ground control points) and the SfM processing (e.g. camera calibration and
87 orientation).

88 Giordan et al. (2015) proposed two different kinds of RPAS-DP surveys for landslide
89 applications (Fig. 2): (a) RPAS-DP survey for steep slopes (slope angle $>40^\circ$, usually rock
90 slopes) and (b) RPAS-DP survey for moderate to gentle slopes (slope angle $<40^\circ$). These two
91 kinds of survey differ by camera view direction. When conducting the survey, an oblique or
92 even horizontal camera view may work best for steep slopes whereas a vertical or nadir camera
93 view is typically best for gentle slopes. A multirotor RPAS is often used for steep slopes while
94 multirotor or fixed-wing RPAS can be used for gentle slopes. This conceptual differentiation
95 of RPAS surveys can be applied not only to landslide studies but also to other geological studies
96 in similar terrain.



97
98

99 Fig. 2. Different RPAS survey options proposed by Giordan et al. (2015) for (a) steep rock
100 slopes and (b) gentle to moderate slopes.

101 In geoscience applications, the DSM and orthoimage can be managed with GIS software and
102 base-level computers. However, the PC and TDOM typically requires specific 3D rendering
103 software and a computer with a medium to high-level graphics card. Usually, due to the
104 presence of a large amount of information, a TDOM requires a higher graphics card
105 performance than a PC. For the analysis of discontinuities in a rock outcrop, a PC or TDOM
106 are required because they allow for selection of 3D point positions that belong to a discontinuity
107 thus allow for a fitting of a plane to a set of points representing the discontinuity. Whereas a
108 PC is composed of 3D points, TDOMs are 3D meshes consisting of triangular facets filled with

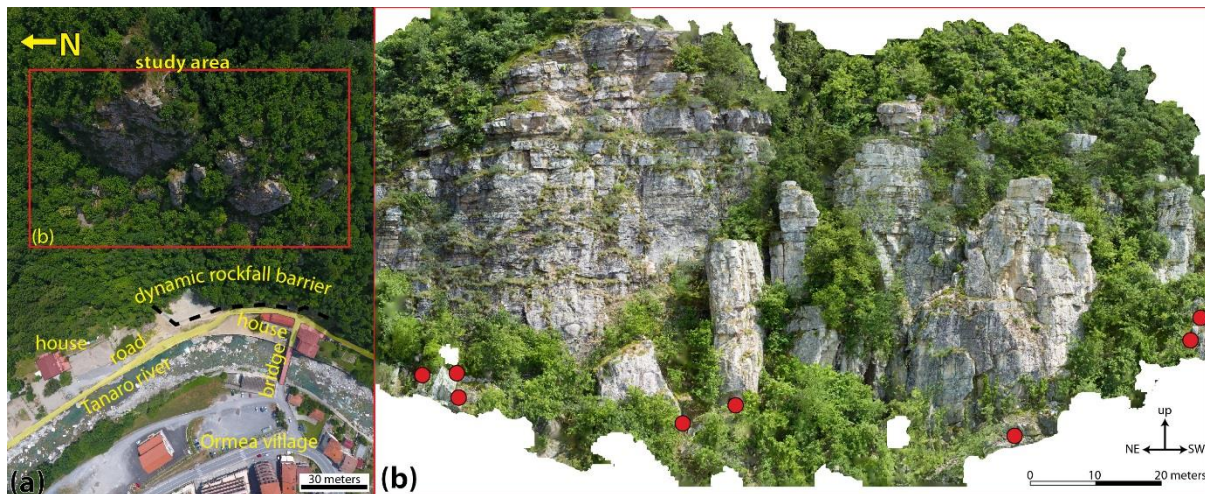
109 image texture in the space between the points defining the facet vertexes. Therefore, a TDOM
110 can significantly improve the identification and the correct interpretation of discontinuity traces
111 that cannot be detected in a PC.

112 The detection of discontinuities in a DOM can be done manually or automatically. Recently,
113 several different algorithms for the semi-automatic detection of discontinuities have been
114 proposed, such as DSE (Riquelme et al., 2014) and qFacet (Dewez et al., 2016), etc. Most of
115 these methods work on a PC and use an algorithm of the k-nearest neighbor (knn).

116 In this study, RPAS-DP was used as a tool to identify and map the discontinuities contained
117 within a sub-vertical rock slope. The rock slope has a complex geometry, and it generates
118 rockfalls. The discontinuity detection was done using both manual and automatic methods, and
119 the results from each method are compared in terms of discontinuity geometry and kinematic
120 instability analysis. The case study demonstrates a workflow for the detection of discontinuities
121 in a sub-vertical rock slope.

122 **2 Study site**

123 The study area is located in the western portion of the Ligurian Alps, near the village of Ormea
124 (CN, Italy), along the Tanaro Valley (44.147° lat., 7.919° long.). On the right side of the river,
125 a vertical rock slope characterized by recurrent instability phenomena imperils roads, a bridge,
126 some houses, and the riverbed that are just below it (Fig. 3).



128 Fig. 3. RPAS-based images: (a) nadir image of the rock slope and the village below and (b)
 129 orthorectified image of the rock outcrop. Red dots indicate the position of the control planes
 130 measurable in the field and visible and measurable in the images acquired by RPAS.
 131

132 The rock slope is approximately 100 m wide and 80 m high and is composed principally of
 133 quartzites. The studied area is characterized by the presence of several large joints at the base
 134 of the slope that can cause the collapse of large sections of the rock bluffs, especially in the
 135 central sector. These joints are monitored by ARPA Piemonte (Regional Environmental
 136 Protection Agency), and some movements were registered after a flood event that occurred in
 137 the Piemonte in November 2016. Furthermore, some unstable blocks were detected in the
 138 southwestern sector immediately after the flood. For this reason, some blocks were removed,
 139 and rockfall nets were installed at the base of the slope.

140 The field investigations were conducted with a goal to measure the main joint sets and to
 141 identify the most unstable areas. Due to the presence of inaccessible unstable sectors of the
 142 rock wall, an innovative solution that considered the use of remote sensing techniques was
 143 evaluated for a better characterization of these areas. The complex geomorphology,
 144 topography, and the existence of trees at the site, immediately highlighted the main limitations
 145 of terrestrial photogrammetry and laser scanning. These methods were only able to acquire data
 146 for limited portions of the slope. In addition, the presence of potential unstable blocks limited
 147 safe access to the entire slope for a manual acquisition of discontinuities. For this reason, the
 148 use of RPAS was considered a good solution for the acquisition of a nadir and oblique dataset
 149 (Fig. 3).

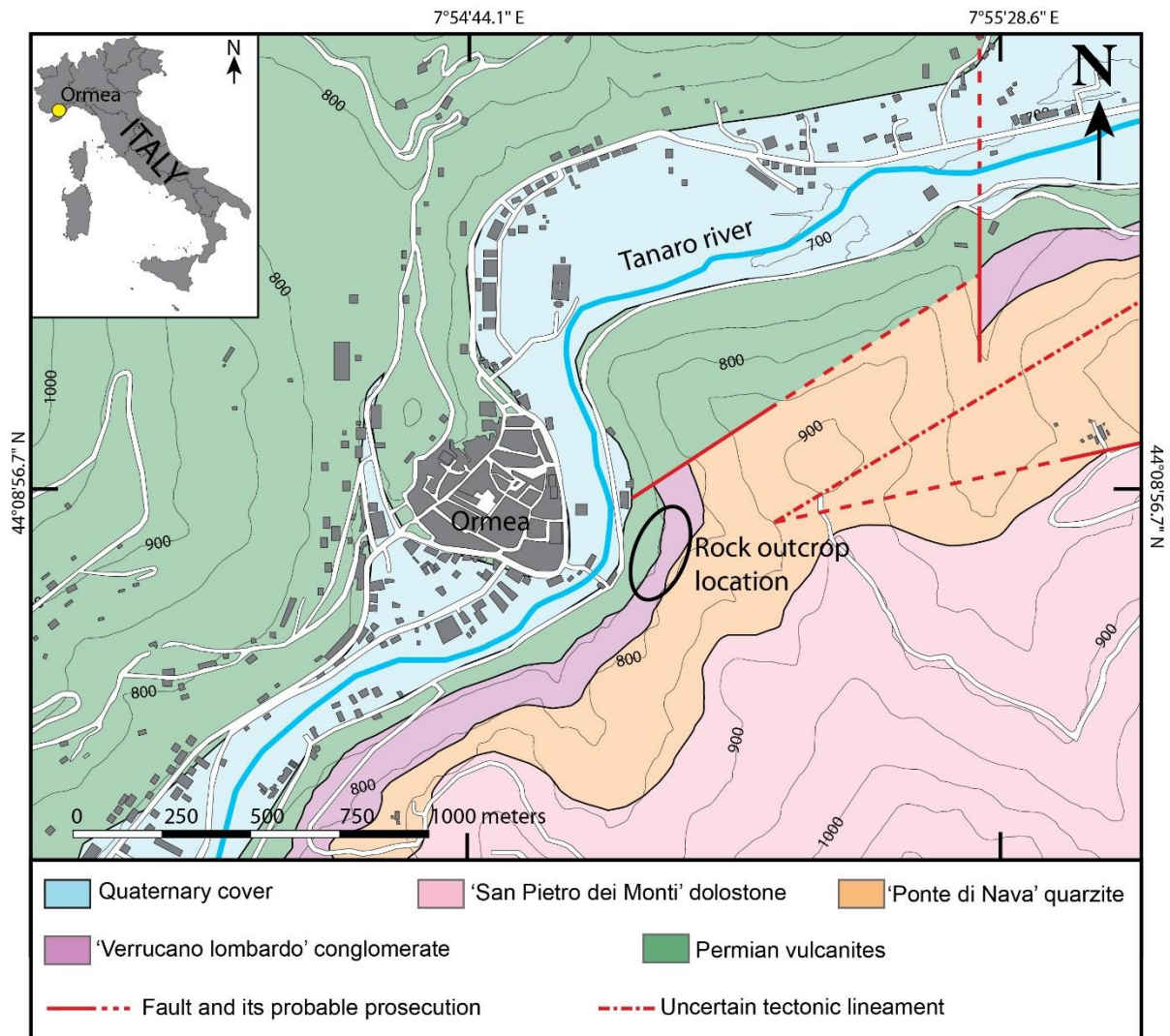
150 2.1 Geology

151 In the Ormea area, the different geological units that compose the central Ligurian Alps
152 (External and Internal Briançonnais, Pre-Piedmont and Piedmont Ligurian units) are stacked
153 upon each other (Fig. 4). The slope that was examined is formed by a succession of rock
154 belonging to the lower part of the External Briançonnais. These lie over a Pre-Namurian
155 metamorphic basement and the clastic Permian succession of the Ollano Formation, which are
156 not exposed in the area. The following lithological units are present:

- 157 • Melogno Porphiroids (Early Permian) – calc-alkaline rhyolitic and rhyodacitic volcanic
158 ignimbrites and pyroclastics.
- 159 • Verrucano Formation (Late Permian) – well-rounded polygenic conglomeratic continental
160 deposits, strongly cemented, with interbedded green and violet schists and whitish
161 conglomerates and sandstones. The formation rests paracomformably on the eroded top of
162 the volcanic complex of the Melogno Porphiroids.
- 163 • Ponte di Nava Quartzites (Early Triassic) – coarse-grained grey quartz arenites and
164 conglomerates with fining-upwards cycles. The lower part of the formation is
165 characterized by a coarser facies with rough bedding, while the upper part is composed of
166 thinner beds of medium-to-fine quartz arenites interbedded with greenish pelites.
- 167 • San Pietro dei Monti Dolomite (Ladinian) – massive to well-bedded grey dolostones and
168 limestones forming a thick carbonate platform succession (about 200 m).

169 Along the right slope of the Tanaro valley, the described succession is tectonically truncated at
170 the level of the San Pietro dei Monti Dolomite by the large sub-horizontal fault that thrusts the
171 Inner Units (Internal Briançonnais, Pre-Piedmont, and Piedmont Ligurian units) over the
172 External Briançonnais.

173 The rock cliff in the study area contains sub-horizontal bedding and large sub-vertical
174 discontinuities that delineate rocky pinnacles characterized by rockfalls and instability
175 phenomena. To the north of the cliff, some NE to ENE tectonic lineaments were detected by
176 the analysis of two sets of aerial photographs and partially verified by field surveys (Fig. 4).
177 One of them coincides with a fault that borders the Melogno Porphiroids.



178
179 Fig. 4. Geological map of the study area.

180 3 Methodology

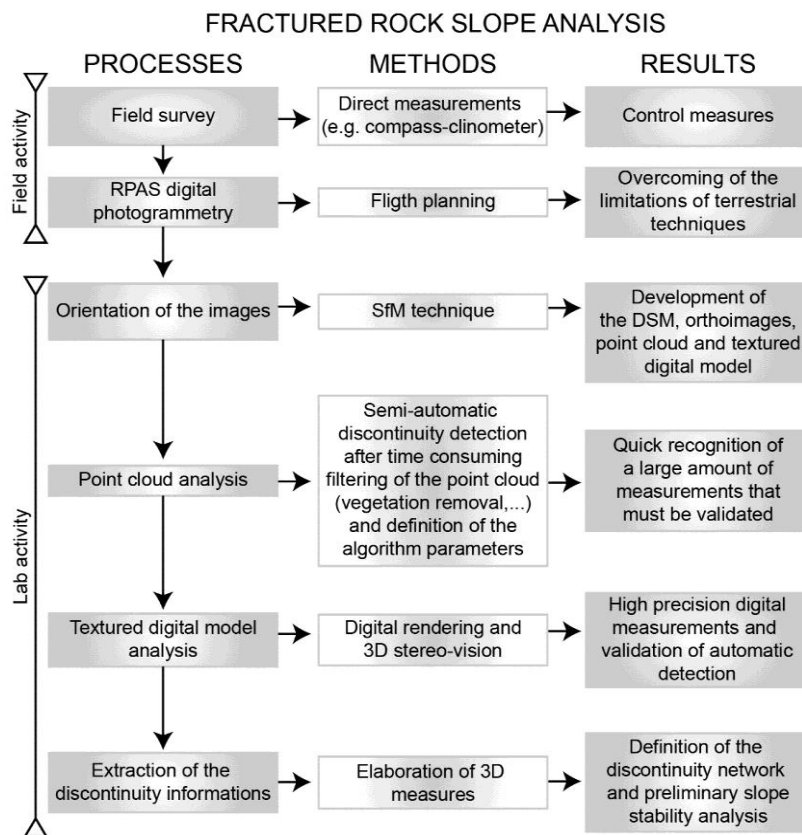
181 A RPAS was used to acquire a series of high-resolution images of the inaccessible rock cliff
182 that is characterized by a complex geometry with several areas that cannot be seen from the
183 ground level. The images were then converted into a TDOM using Structure-from-Motion
184 (SfM) software.

185 A classic field survey with a geological compass-clinometer was performed to measure 145
186 discontinuities in a lateral part of the slope, where the field conditions allowed for safe manual
187 acquisition of direct measurements. Differences between the compass-based field
188 measurements of the orientations of the control planes and discontinuities and the orientations

189 extracted from the TDOM were evaluated. We also measured the orientation of 8 control planes
 190 found near the toe of the rock slope. These planes were also visible in images acquired by
 191 RPAS. This dataset was used to evaluate the accuracy of the discontinuities identified in the
 192 TDOM, and were used to validate the TDOM orientation without the use of GCPs.

193 Discontinuity analysis using the TDOM was done with semi-automatic and manual mapping
 194 methods. In this paper, we present the results from both approaches, and we propose a
 195 composite method for discontinuity identification that involves manual validation of
 196 preliminary automatic mapping results. In particular, the manual mapping using the highly
 197 detailed TDOM allows for the recognition of discontinuities that are orthogonal to the rock
 198 wall and that are often identifiable only as traces without 3D relief and no visible plane surfaces
 199 (Seers and Hodgetts, 2016; Biber et al., 2018). For this reason, the semi-automatic methods
 200 based on the coplanarity test of the points of the PC can often underestimate these geological
 201 structures (e.g. Dewez et al., 2016).

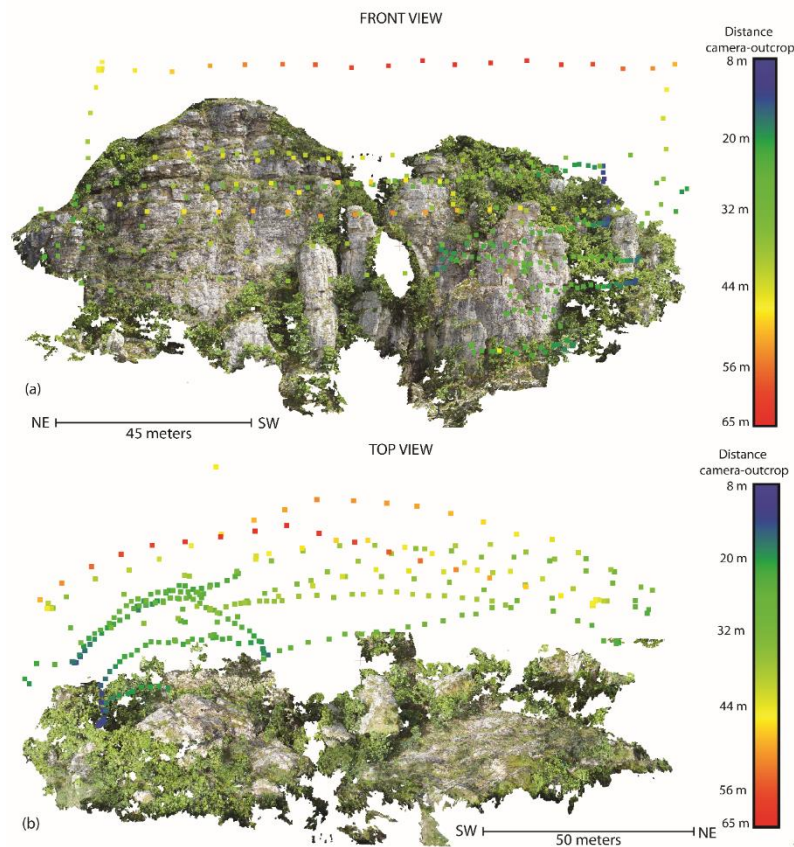
202 The main steps of the proposed methodology are schematically indicated in Fig. 5.



203
 204 Fig. 5. Conceptual scheme of the proposed workflow.

205 **3.1 RPAS digital photogrammetric survey and image processing**

206 The RPAS-based digital photogrammetric survey was conducted with an oblique orientation
207 for the on-board camera and 236 digital photographs were acquired. The collected images had
208 a minimum overlap and sidelap of about 90% and 80%, respectively. In order to capture the
209 complex geometry of the outcrop and to improve the precision of the generated TDOM, the
210 images were acquired from positions parallel (strips of photographs taken along a fly line) and
211 convergent to the outcrop (Birch, 2006). The average distance from the camera to the closest
212 rock surface was 32 m, with a standard deviation of 11 m (Fig. 6). The flights were flown under
213 manual control in a sequence of back-and-forward flight lines to cover the full vertical extent
214 of the rock outcrop.



215

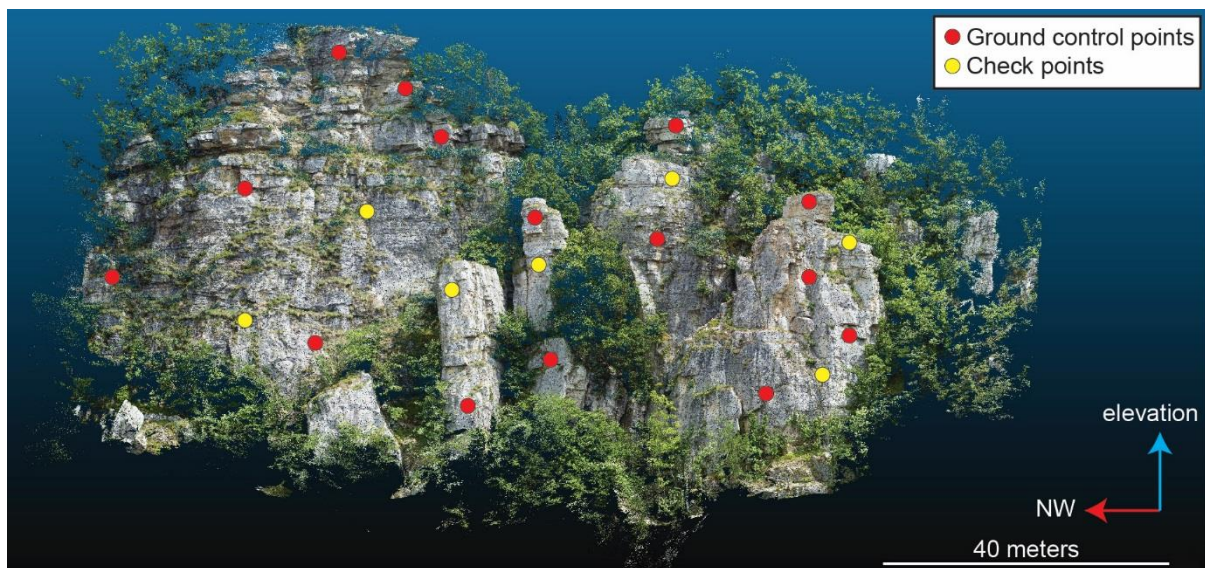
216 Fig. 6. Front and top view of the rock outcrop showing the camera locations. Point colors
217 indicate the camera-outcrop distance.

218 The features of the RPAS platform and on-board camera are reported in Table 1.

219 Table 1. RPAS and on-board camera specifications.

RPAS system specifications					
RPAS type	Dimension	Engines	Rotor Diameter	Empty weight	Payload
V-shaped quadcopter	56 x 80 x 17 cm	4 brushless	381 mm	6.9 kg	8.3 kg
On-board camera specifications					
Camera	Sensor type	Sensor size	Image size	Pixel size	Focal length
SenseFly Albris	CCD	10 × 7.5 mm	7152 × 5368 px	1.4 x 1.4 μm	8 mm

220 The RPAS was equipped with a GNSS/IMU and all the acquired images were georeferenced
 221 in a WGS84/UTM32N metric coordinate system. Moreover, to obtain a high accuracy model
 222 22 points on the slope were measured with a **total station** Topcon GPT-7001L total station (15
 223 were used as Ground Control Points – GCPs - and 7 as Check Points - CKPs). The GCPs and
 224 CKPs positions are shown in Figure 7. The GCPs network was georeferenced using four
 225 different points acquired by the robotized total station and a Leica 1200 GPS RTK.



226
 227 Figure 7. 3D Point cloud of the rock slope. Red and yellow dots indicate the position of GCPs
 228 and CKPs, respectively.

229
 230 The TDOMs or 3D digital models were created with the Structure-from-Motion (SfM)
 231 technique using Photoscan Professional v.1.2.5 software (Agisoft, 2016), which is widely

232 employed in earth sciences studies (e.g. Turner et al., 2014; Goncalves and Henriques, 2015;
233 Casella et al., 2016; Cawood et al, 2017; Jordá Bordehore et al., 2017; Salvini et al., 2017).
234 Due to the presence of the 22 GCPs acquired using a total station we decided to develop two
235 different 3D models. The procedures used during the processing were the same for the two
236 models, except for the use of GCPs for the ~~direct~~-georeferenced model versus **georeferencing**
237 using only the RPAS on-board GPS. For a detailed description of the technique, see Lucieer et
238 al. (2013) and Turner et al. (2014). The processing steps are summarized below.

239 *Image pre-processing.* All the 236 images were georeferenced using the coordinates registered
240 by the on-board GPS; 12 images with blur effects were discarded.

241 *Image matching, bundle block adjustment, and creation of sparse PC.* 224 images were aligned
242 using the highest accuracy (full resolution matching) and using the pair pre-selection method
243 that takes into account the image positions registered by the RPAS-GPS. Then the bundle block
244 adjustment was computed using the positions of the 15 GCPs measured using the total station.
245 The accuracy of the GCPs was imposed as 50 mm. A sparse PC of 505081 points was obtained.

246 *Dense PC creation.* Due to the resolution of the images (38 Mpx), the dense PC was developed
247 using the *high* quality parameters of the Photoscan procedure (i.e. all the images were
248 subsample for a factor 2 in each dimension), and a *mild* depth filtering. A dense PC of ~98
249 million of points was generated at the end of the process. The mean surface density of the PC
250 was around 1000 points per m².

251 *Mesh creation.* After a manual removal of the highly vegetated areas, a 3D mesh was
252 constructed selecting the *high* face count suggested by the software. A mesh with ~35 million
253 faces for a total surface of 12744 m² was developed at the end of the process.

254 *Texture mapping and orthophoto mosaic generation.* A *generic* texture mapping and a *mosaic*
255 blending mode were used to obtain the texture for the mesh, considering only the images with
256 a quality value > 0.7 and developing a texture atlas composed of 10 files with 8 Mpx. Finally,
257 an orthophoto mosaic (Fig. 3b) with a resolution of 6.45 mm/pixel was generated as a TIFF
258 file.

259 *Export of PC and TDOM.* The PC and TDOM were exported using a WGS84 metric coordinate
 260 system. In particular, the dense PC was exported as a xyz.txt file including the RGB color value
 261 for each point. The TDOM was exported as an OBJ file including the vertex normal and texture.

262 3.2 Accuracy

263 The absolute accuracy of the two DOMs (one directly georeferenced using the on-board GPS
 264 coordinates and the other by means of 22 GCPs and check points widely distributed across
 265 the target area) were calculated by comparing GCPs and check point coordinates measured
 266 by the total station and with coordinates of the same points in the models (Table 2).

267 Table 2. Absolute accuracies of GCP and directly georeferenced models evaluated on 15
 268 GCPs and 7 CKPs.

	DOM GCP-georeferenced				DOM directly georeferenced	
	GCP errors (m)		CKP errors (m)		GCP and CKP errors (m)	
	Horizontal	Vertical	Horizontal	Vertical	Horizontal	Vertical
Mean	0.023	0.015	0.033	0.009	0.807	9.401
St. Dev.	0.012	0.012	0.023	0.005	0.136	0.208
Min	0.005	0.001	0.008	0.004	0.611	9.005
Max	0.039	0.049	0.082	0.019	1.097	9.719

269

270 The comparison shows a satisfying absolute accuracy of the GCP-model, while the model
 271 that is directly georeferenced using the on-board GPS coordinates for each photograph is
 272 affected by a significant shift, especially in altitude. A shift or translation of the model
 273 coordinates is commonly observed when using just the coordinates from the RPAS GPS as
 274 these tend to be incorporate an off-set from the actual coordinates. While the RPAS GPS
 275 coordinates may be shifted from the actual coordinates, the relative positioning of the
 276 coordinates is typically far more accurate. The relative accuracy of the directly
 277 georeferenced model was evaluated by comparing the lengths and azimuths of vectors joining
 278 pairs of points in the model with the corresponding lengths and azimuths from the GCP-
 279 georeferenced model. The maximum angular differences in attitude (Table 3) and length of
 280 20 measured vectors are $\pm 1^\circ$ and 0.3%, respectively. Similarly, a comparison of 11 plane
 281 attitudes on both models (Table 3) shows a maximum angular difference of $\sim 1^\circ$.

282 Table 3. Relative accuracies of TDOMs evaluated by angular differences in attitude of 20
 283 measured vectors and 11 plane attitudes.

	Lines errors			Planes errors		
	Trend	Plunge	Angle	Dip	Dip Azimuth	Angle
N° of measures	10	10	10	11	11	11
Mean	1.0	1.2	1.6	0.8	0.5	1.0
St. Dev.	0.4	1.2	1.6	0.4	0.2	0.4
Min.	0.3	0.1	0.2	0.3	0.2	0.4
Max.	1.7	3.3	5.7	1.5	1.0	1.8

284

285 Moreover, to validate the results of the RPAS survey, the control planes manually identified
 286 using the TDOM were compared with those measured in the field with a geological compass.
 287 During the field survey, only a small number of control planes were measured at the toe of
 288 the slope because the rest of the outcrop was largely inaccessible and unsafe to work on. The
 289 field-measured control planes were chosen because they were clearly visible from the RPAS
 290 survey.

291 The mean angle between the orientations of the control planes determined directly in the field
 292 and those measured manually from the TDOM was 3°, with a maximum of about 6° (Table
 293 4). This value suggests that both methods gave similar results given that the typical precision
 294 obtained for field collection of discontinuity orientations by a compass is typically between
 295 2° and 5°. Moreover, manual sampling can be affected by an orientation bias due to the local
 296 variation of surface orientations, whereas DOM sampling often overcomes this problem
 297 because the best-fit plane covers a larger surface area of the discontinuity.

298 Table 4. Comparison between the dip direction/dip ($^{\circ}$) of the control planes measured directly
 299 on the outcrop (average measurement for a single control plane) and those acquired by
 300 manual detection on TDOM.

Plane	Compass	No. measurements	TDOM	Angle between planes ($^{\circ}$)
a	039/69	10	043/75	6.1
b	040/72	8	043/73	1.3
c	040/70	11	043/70	1
d	039/78	13	44/79	5
e	227/80	8	228/85	5.1
f	180/82	6	180/78	4
g	041/86	15	043/87	1
h	226/87	6	221/88	1

301

302 These results confirm the validity of the DOMs. For geological outcrop studies, having a
 303 model that is at the correct scale and orientation is certainly more important than having it
 304 precisely georeferenced because the measurements (e.g., attitudes of plane and surfaces)
 305 calculated in a DOM characterized by good relative accuracy are equivalent to measurements
 306 made on the outcrop.

307 **3.3 Discontinuity Analysis**

308 Automatic and semi-automatic procedures to identify and map discontinuities have been
 309 developed and used by several authors (Slob et al., 2004; Jaboyedoff et al., 2007; Vöge et al.,
 310 2013; Gigli and Casagli, 2011; Chen et al., 2016; Dewez et al., 2016; Gomes et al., 2016; Jordá
 311 Bordehore et al., 2017; Guo et al., 2017) and represent important improvements in the use of
 312 digital terrain models and/or point-clouds. In this paper, we present the results obtained by
 313 manual and semi-automatic procedures, and we show the impact that these two approaches can
 314 have on the identification of discontinuity sets and potential instabilities.

315 *3.3.1 Manual detection and mapping of discontinuities*

316 The manual recognition and measurement of the discontinuities were conducted by visualizing
317 and analyzing the TDOM in a stereoscopic environment using a Planar Stereoscopic Mirror
318 SD2220W device. This device has two separate display monitors placed one above the other
319 in a clamshell configuration with a half-silvered glass plate bisecting the angle between the two
320 displays. It is important to emphasize that the identification of the discontinuities was realized
321 by the stereoscopic inspection of the images texturized on the 3D model and not only by
322 examining the point cloud. In fact, the stereo-vision of the texturized model (i.e. examining the
323 real photographic images of the outcrop) allows for a better understand the real nature and
324 geometry of the structures to be analyzed (strata, discontinuities, traces of fractures, lineations)
325 and avoids misinterpretation due to 2D visualization on standard monitors of 3D objects
326 depicted by a point cloud.

327 The measurement of planes that represent discontinuities was performed using the tools in the
328 open-source software CloudCompare v.2.9. After the visual identification of a discontinuity,
329 the points in the cloud belonging to the discontinuity were digitized, and the 3D discontinuity
330 plane to these points was determined using a least-squares best-fit approach. Several
331 measurements were collected for each discontinuity plane or trace, and the average
332 measurement was taken to represent the discontinuity geometry.

333 The discontinuities were sampled for their entire visible exposure as planes and/or traces to
334 calculate not only their orientation (dip and dip direction) and position, but also their
335 dimensions (discontinuity length).

336 To evaluate the robustness of the manual detection results obtained using the free software
337 CloudCompare, we repeated the manual mapping of discontinuities using a different
338 commercial software. Another operator used 3DM Analyst© photogrammetric software
339 (ADAM Technology) to identify the discontinuities in the same studied area. 3DM Analyst©
340 has a dedicated application for the identification and mapping of discontinuities that helps the
341 operator to map them easily. In this work, we started from the same image dataset and created
342 a digital model using the procedure proposed by ADAM. At the end of the model generation,
343 32 stereo-pairs were selected to have a complete 3D representation of the studied area. The 32

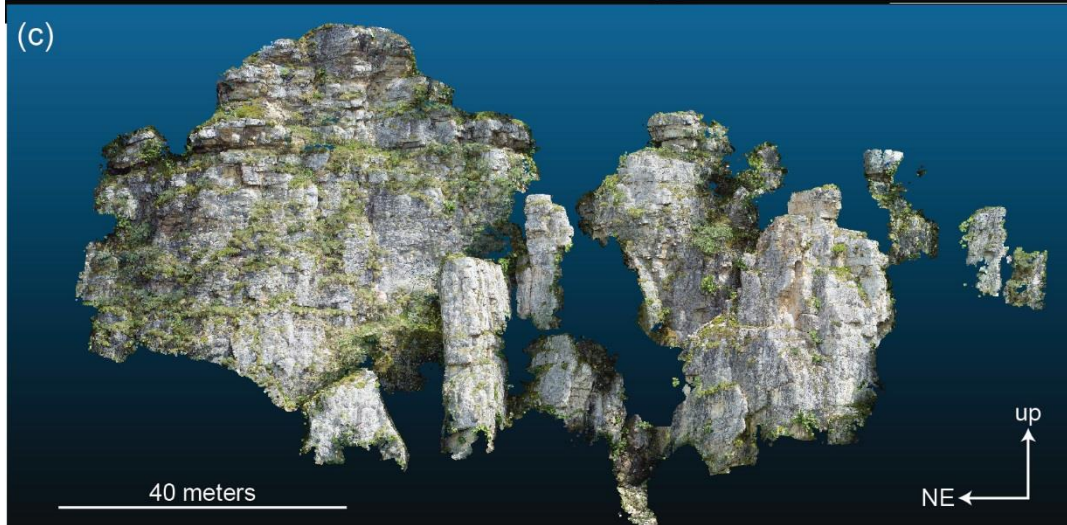
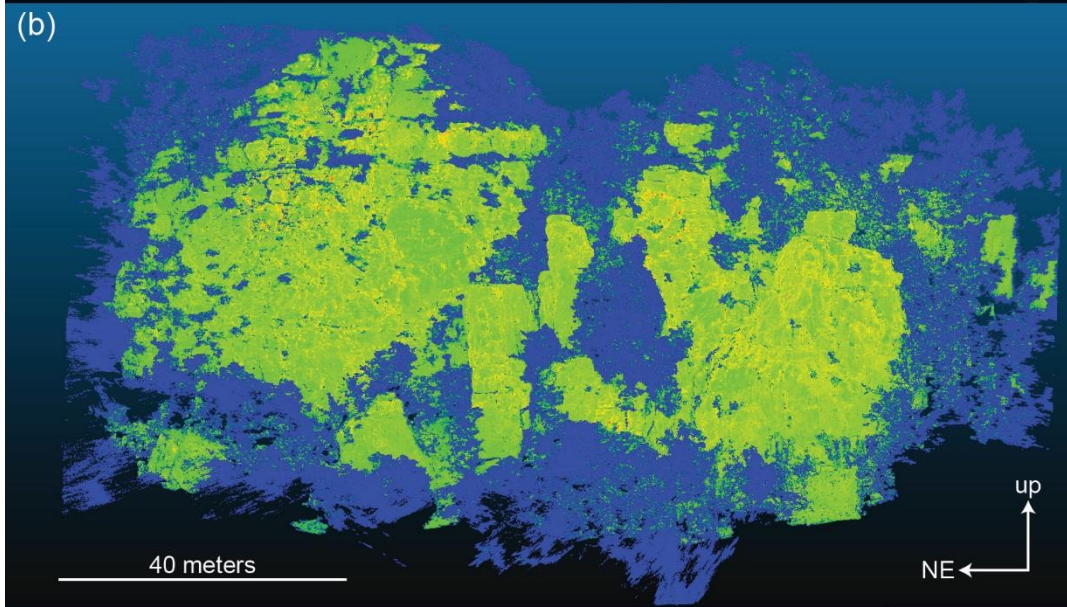
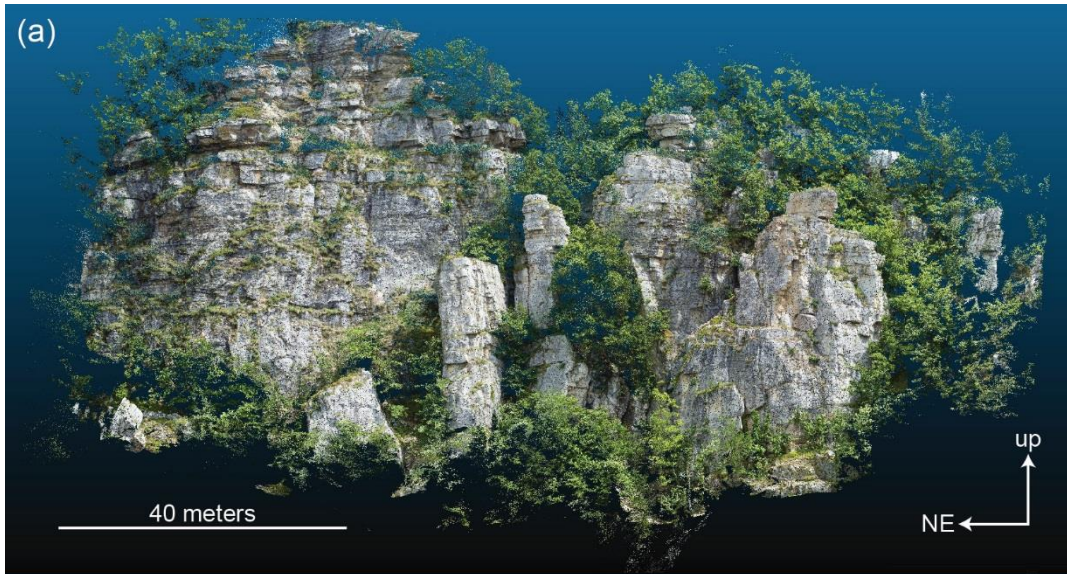
344 stereo-pairs provided a 3D view of the studied area that was used to detect and map the
345 discontinuities. The obtained results are compared in Chapter 4.

346 3.3.2 *Semi-automatic detection of discontinuities*

347 The point cloud generated using the SfM-based photogrammetric procedure in Agisoft
348 Photoscan was analyzed with three different open-source algorithms for the semi-automatic
349 detection of discontinuities: i) Discontinuity Set Extractor (DSE) proposed by Riquelme et al.
350 (2014), ii) qFacet Fast Marching and iii) qFacet Kd-tree. The second and third algorithms are
351 plugins for CloudCompare proposed by Dewez et al. (2016).

352 The first method identifies and defines the algebraic equations for different planes by applying
353 an analysis based on a coplanarity test on neighboring points, finding principal orientations by
354 Kernel Density Estimation, and identifying clusters by the Density-Based Scan Algorithm with
355 Noise (see Riquelme et al., 2014 for details). The other methods are based on two algorithms
356 (qFacet Fast Marching and qFacet Kd-tree) that divide the initial point cloud into sub-cells,
357 compute elementary planar objects, and then progressively aggregate the planar objects
358 according to a planarity threshold into polygons. The boundaries of the polygons are adjusted
359 around segmented points with a tension parameter, and the facet polygons can be exported as
360 3D polygon shape files. See Dewez et al. (2016) for details.

361 As a preprocessing step to improve the results of the semi-automatic detection, we removed
362 from the point cloud all points that belong to vegetation. Two filter procedures were applied:
363 the first is based on color attributes of the points (RGB, hue, saturation, etc.) and was
364 implemented in Agisoft software, while the second was performed by masking the sectors with
365 a lower density of points that characterize the vegetated areas (Fig. 8). It was impossible to
366 completely remove all points corresponding to vegetation, especially in areas of sort dry grass
367 and small shrubs. Thus their presence in the final point cloud may affect the correct recognition
368 of discontinuities.



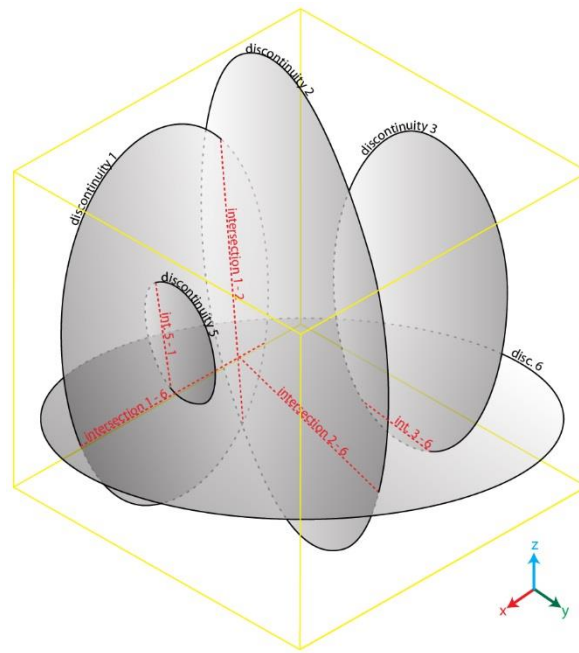
370 Fig. 8 Vegetation removal process: (a) initial point cloud, (b) classification of points for
371 removal (blue areas) based on RGB attributes of the points and the low density of the PC in
372 vegetated areas, (c) final PC obtained after the use of the filters.

373 The semi-automatic detections of the discontinuities were performed on a PC characterized by
374 a point surface density of approximately 10386 points per m² (mean spacing between points
375 approximately 10 mm). The parameter settings used in the different algorithms for the
376 automatic detection of the discontinuities are described in Section 4.2.

377 3.3.3 *Rock slope kinematic analysis*

378 A stereonet-based kinematic analysis of the main rock slope failure mechanisms (planar
379 sliding, wedge sliding, flexural toppling, and direct and oblique toppling) was performed on
380 the discontinuity systems detected by the manual and automatic analyses to highlight the
381 possible differences and inconsistencies. The kinematic analyses assumed a friction angle of
382 30° and a lateral limit value (Goodman, 1980; Hudson and Harrison, 1997) of ±20° from the
383 dip direction of the outcrop face.

384 Whereas the planar sliding and flexural toppling kinematic analyses were performed using the
385 orientation of all identified discontinuities, the wedge sliding and direct and oblique toppling
386 kinematic analyses used the detected intersections between the identified discontinuities. The
387 intersections were calculated considering the discontinuities as circular objects with a diameter
388 equal to the maximum extension of the discontinuity trace and/or plane measured on the
389 TDOM and considering its position in 3D space (Fig. 9). Due to the good exposure of the
390 outcrop, the estimate of the maximum extension of the fractures can be considered reliable. If
391 two discontinuities cross each other, a discontinuity intersection is calculated and plotted on
392 the stereonet by its trend and plunge. The kinematic analysis was first performed for an overall
393 slope face dipping 75° towards 300°.



394

395 Fig. 9. Example showing lines of intersection of circular discontinuities.

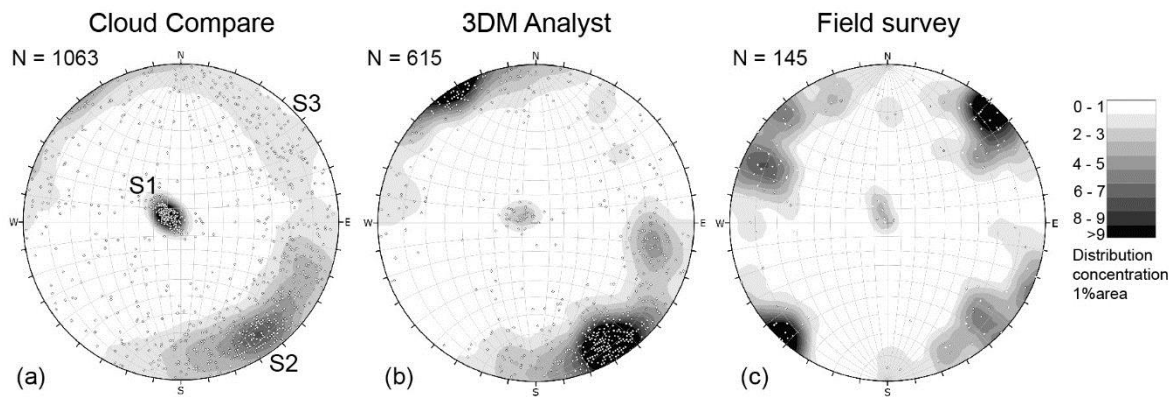
396 4 Results

397 The results from using the different discontinuity detection methods are presented in this
 398 section along with results from kinematic analyses of different possible structurally-controlled
 399 failure mechanisms. The purpose of this section is to compare and contrast the different
 400 discontinuity detection methods and their influences on the subsequent failure mode analyses.

401 4.1 Manual detection of discontinuities

402 The manual analysis of the TDOM representing the rock slope identified 1036 discontinuities
 403 using Cloud Compare. The availability of a high-resolution 3D model was very useful for the
 404 recognition of discontinuities with different orientations. In particular, the texture of the model
 405 supported the identification of discontinuities that are orthogonal to the rock wall. These
 406 discontinuities can be very difficult to detect when examining only the point-cloud.

407 In Fig. 10 we present the measurements of the discontinuities manually obtained using Cloud
 408 Compare, those acquired by another operator that analyzed the same image dataset by 3DM
 409 Analyst© photogrammetric software, and those achieved during a field survey conducted in
 410 two accessible positions of the rock slope using a compass-clinometer.



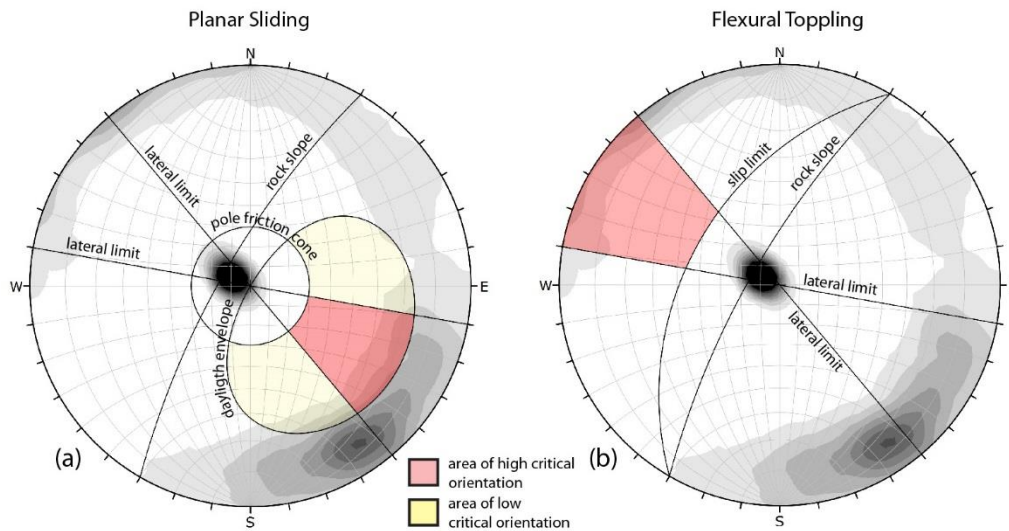
411

412 Fig. 10 Comparison of the discontinuity orientation (stereographic projections – equal angle,
 413 lower hemisphere) measured by (a) Cloud Compare, (b) 3DM Analyst software, and (c) field
 414 survey; the main discontinuity sets are indicated in (a).

415

416 Fig. 10 clearly shows that all approaches recognize 3 sets of discontinuities. The dominant
 417 discontinuity set (S1) is the bedding, which is sub-horizontal. Nearly vertical, cross-cutting
 418 joints that are roughly perpendicular to the bedding are also common. These cross-cutting joints
 419 have a wide range of strikes, and they can be subdivided into different subsets (S2 and S3).
 420 The results from the three approaches are similar, and therefore for the remainder of this paper,
 421 we consider only the dataset (1036 measurements) obtained using CloudCompare, a freely
 422 available open-source software.

423 The kinematic analysis for a planar sliding mechanism indicates that 10% of the discontinuity
 424 planes (essentially formed by random discontinuities) could act as a sliding surface (Fig. 11a).
 425 The critical discontinuities for a flexural toppling failure mechanism (Fig. 11b) consist of about
 426 4% of the total detected discontinuities and were essentially due to discontinuities in set S2.



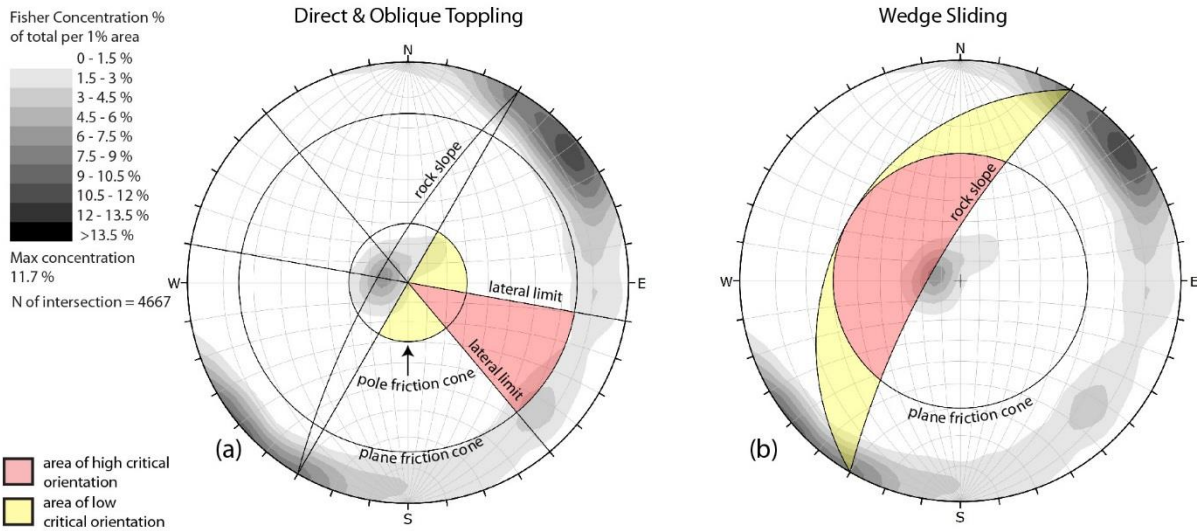
427

428 Fig. 11 Kinematic analysis of possible failure mechanisms involving individual
 429 discontinuities (a - planar sliding and b - flexural toppling). The critical pole locations fall
 430 inside the pink areas (equal angle, lower hemisphere, stereographic projections).

431

432 Starting with the detected discontinuities, 4667 possible intersections were considered for the
 433 identification of possible wedge sliding and toppling (direct and oblique) instabilities. The most
 434 common failure mechanism that was identified from the kinematic analysis (Fig. 12) was
 435 wedge sliding, which involves 12% of the 4667 intersections. In particular, the most critical
 436 wedges are those formed by intersections between discontinuities in sets S2 and S3.

437 The kinematic analysis of the direct and oblique toppling failure mechanisms indicates that 7%
 438 of the discontinuity intersections could be critical for the block toppling mechanism (2% for
 439 direct toppling and 5% for oblique toppling).



440

441 Fig. 12 Kinematic analysis of possible failure mechanisms involving intersections between
 442 discontinuities (a - direct and oblique toppling and b - wedge sliding). The critical
 443 intersection locations fall inside the pink areas.

444 4.2 Semi-automatic detection of discontinuities

445 4.2.1 Discontinuity Set Extractor (DSE) algorithm

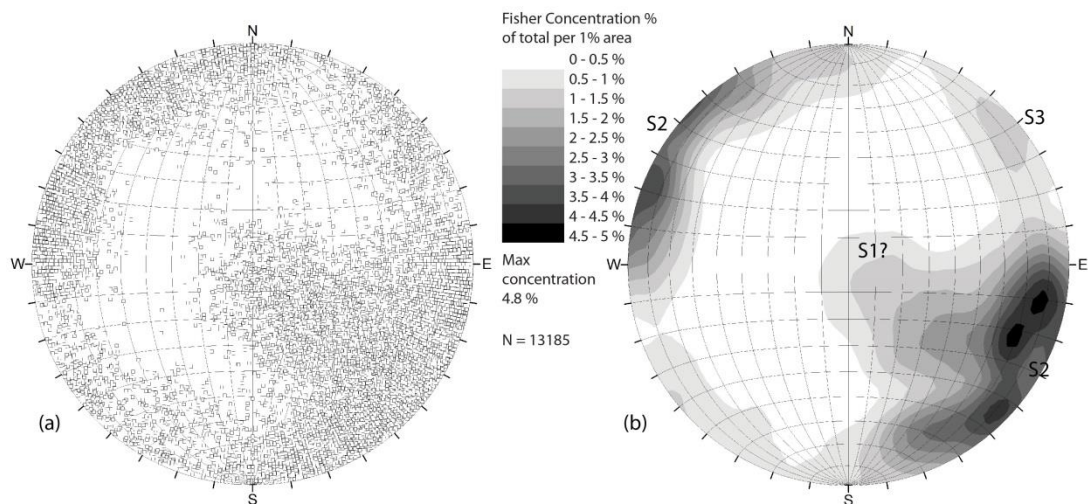
446 The DSE algorithm (Riquelme et al., 2014) was run with Matlab© version 2.0.2 software. This
 447 method detects the structural discontinuities using a 3D point cloud by measuring the attitude
 448 of the outcrop at each point. If the point is surrounded by other coplanar points, the method
 449 statistically determines the orientation of the plane that represents these points. The parameters
 450 used to calculate the normal vector at each point, the density of the poles, and the different
 451 discontinuity sets are defined in Table 5 (see Riquelme et al., 2014 for details).

452 A cluster analysis was performed which considers that all points of a cluster belong to a set if
 453 they have a similar normal vector and setting the parameter $k\sigma = 1.5$ to test whether two clusters
 454 should be merged. Only clusters with more than 100 points are considered as discontinuity
 455 planes.

456 Table 5 Parameters used in the DSE algorithm.

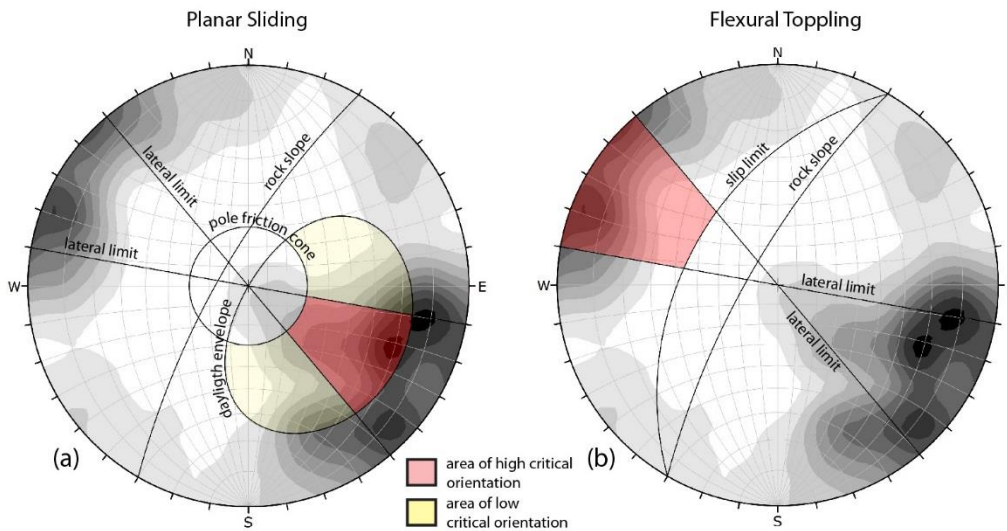
<i>knn</i>	<i>h</i>	<i>nbins</i>	<i>anglevppal</i>	<i>cone</i>	<i>kσ</i>
30	0.2	64	10	30°	1.5

457 The DSE algorithm detected 13185 discontinuity planes in the point cloud. The orientation of
 458 the poles to these planes are plotted in Fig. 13 and they show a high dispersion with the highest
 459 pole concentration occurring in the SE quadrant of the stereonet. It is difficult to assign the
 460 detected discontinuities to distinctive discontinuity sets because of their dispersion. However,
 461 a comparison of these results with the manual mapping shows that the S1 set has lower visibility
 462 and blends into discontinuities from set S2. The DSE algorithm most frequently identified the
 463 steeply dipping discontinuities assigned to set S2. The S2 set has a high orientation dispersion
 464 and appears to include planes dipping at lower angles to the NW. Another minor set of
 465 discontinuities (S3) that steeply dips toward the SW was also found. These discontinuities are
 466 roughly orthogonal to Sets S2 and S1.



467
 468 Fig. 13 Stereographic projection (lower hemisphere, equal area) of the poles to the
 469 discontinuities detected by the DSE algorithm and contour plot of pole concentrations.

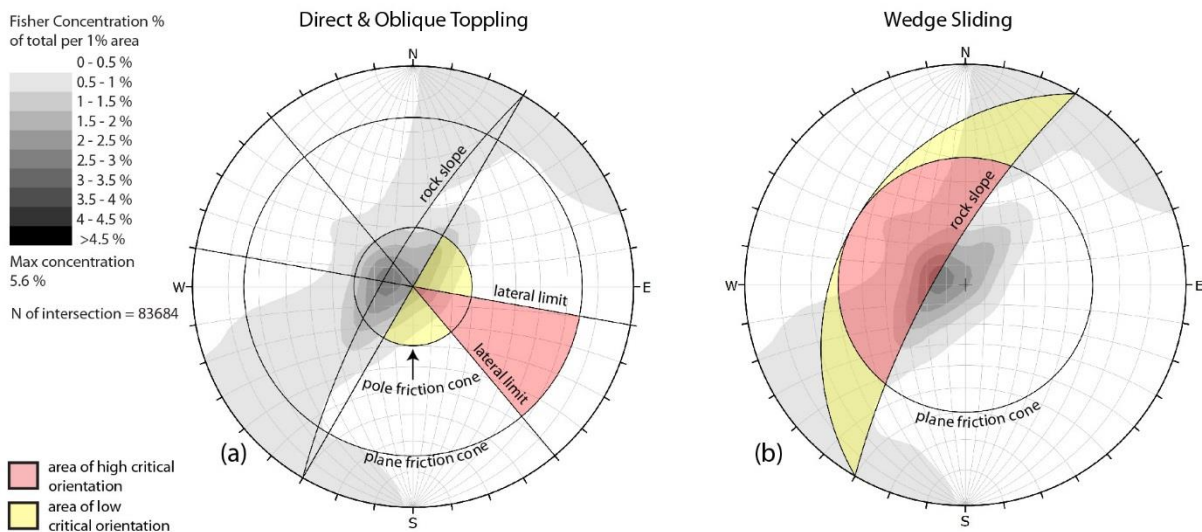
470 A kinematic analysis of possible failure mechanisms suggests that planar sliding (Fig. 14) could
 471 occur on 31% of the 13185 discontinuities. These discontinuities typically occur in set S2
 472 (72%). Flexural toppling (Fig. 14) involves 11% of the total number of the detected
 473 discontinuities, and these belong to set S2.



474

475 Fig. 14 Kinematic analysis of possible failure mechanisms involving individual
 476 discontinuities detected by the DSE algorithm (a - planar sliding and b - flexural toppling).
 477 The critical pole locations fall inside the pink areas (equal angle, lower hemisphere,
 478 stereographic projections).

479 The wedge sliding failure mechanism involves 39% of the 83684 discontinuity intersections.
 480 The critical intersections for wedge sliding involve discontinuities from sets S2 and S3. Direct
 481 and oblique toppling modes involve respectively 2% and 10% of the total number of the
 482 discontinuity intersections.



483

484 Fig. 15 Kinematic analysis of the possible failure mechanisms involving intersections
 485 between discontinuities detected by the DSE algorithm (a - direct and oblique toppling and b
 486 - wedge sliding). The critical intersections fall inside the pink areas.

487 4.2.2 *qFacet Fast Marching (FM) algorithm*

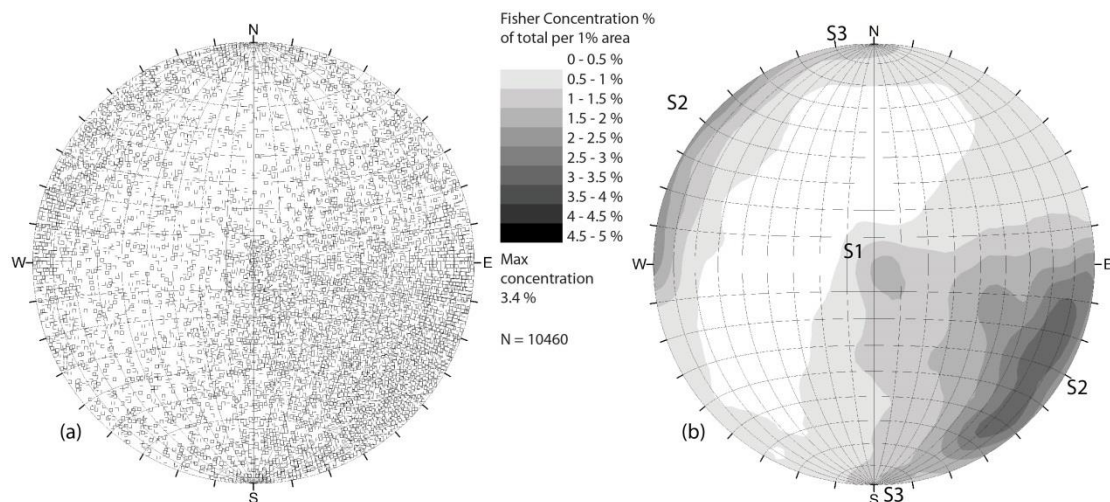
488 The qFacet FM algorithm (Dewez et al., 2015) was run using the CloudCompare v.2.9
 489 software. The qFacet FM algorithm divides the point cloud into clusters of adjacent co-planar
 490 points using a regular lattice subdivision specified by the octree structure, measures the
 491 orientation of elementary facets and groups them into encompassing planes, and classifies
 492 parallel planes into sets.

493 The parameters used to calculate the cell fusion (octree level), the maximum distance of a point
 494 to a best-fitting plane, the minimum number of points per facet, and the maximum edge length
 495 used to extract the plane perimeter are defined in Table 6 (see Dewez et al., 2015 for details).

496 Table 6 Parameters used in the qFacet Fast Marching algorithm.

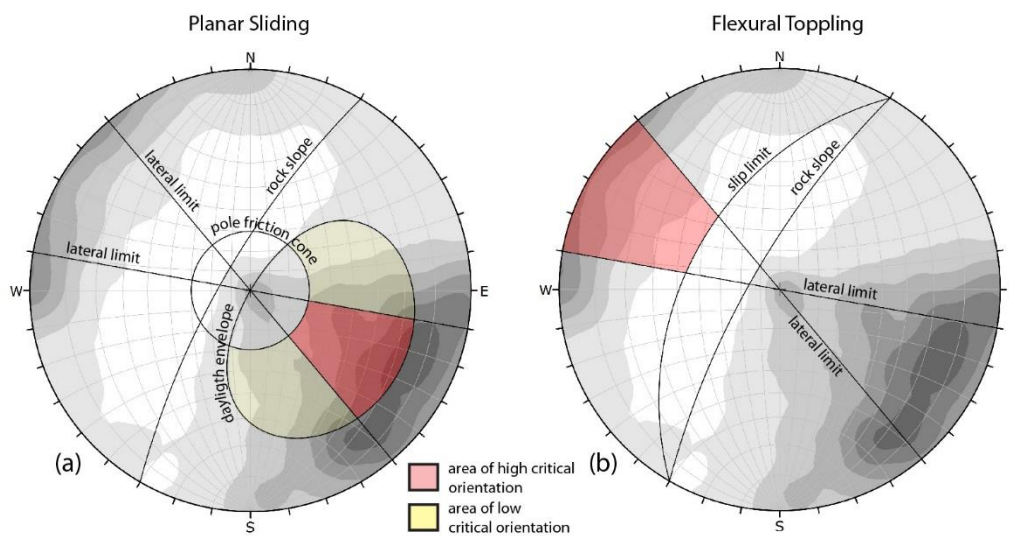
octree level	max distance @ 99%	minimum point per facet	max edge length
8 (0.13 m)	0.1 m	100	0.86 m

497 Using the parameters in the Table 6, the qFacet FM algorithm detected 10460 discontinuity
 498 planes. Similar to the DSE algorithm, the orientation of the poles to these planes (Fig. 16) show
 499 a high dispersion with the highest concentration occurring in the SE quadrant of the stereonet.
 500 Three principal sets of discontinuities can be recognized. The S1 set is sub-horizontal or dips
 501 slightly to the NW. The S2 set dips towards the NW with a dip angle between 50° and 90°. The
 502 S3 set is sub-vertical with a strike of approximately E-W.

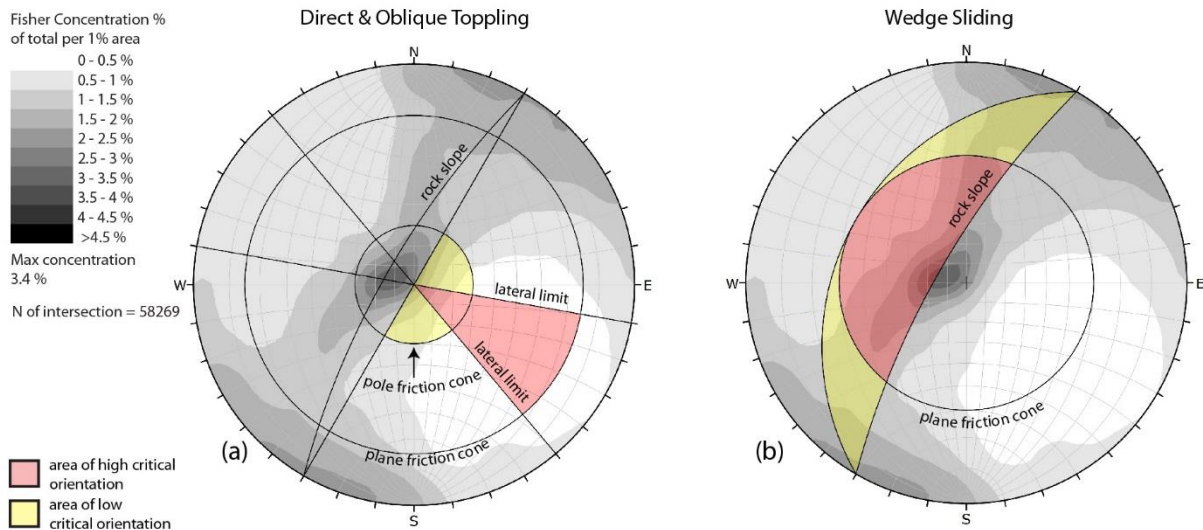


503
 504 Fig. 16 Stereographic projection (lower hemisphere, equal area) of the poles of the
 505 discontinuities detected by the qFacet FM algorithm and contour plot of pole concentrations.

506 A kinematic analysis of potential slope failure mechanisms reveals that planar and wedge
 507 sliding are potentially the most critical mechanisms (Fig. 17 and 18). Planar sliding could
 508 involve 33% of the 10469 discontinuities, essentially those in set S2. Wedge sliding shows that
 509 34% of the 58269 discontinuity intersections could be critical, involving mostly discontinuities
 510 from S1 and S3. A kinematic analysis of the different toppling mechanisms indicates that these
 511 mechanisms should play a minor role in the instability of the rock slope. In particular, flexural
 512 toppling could be caused by 7% of all the detected discontinuities and direct and oblique
 513 toppling could be caused respectively by 2% and 5% of all the discontinuity intersections.



514
 515 Fig. 17 Kinematic analysis of possible failure mechanisms involving individual
 516 discontinuities detected by the qFacet FM algorithm (a - planar sliding and b - flexural
 517 toppling). The critical pole locations fall inside the pink areas (equal angle, lower
 518 hemisphere, stereographic projections).



519

520 Fig. 18 Kinematic analysis of the possible failure mechanisms involving intersections
 521 between discontinuities detected by the qFacet FM algorithm (a - direct and oblique toppling
 522 and b - wedge sliding). The critical intersections fall inside the pink areas.

523 4.2.3 qFacet Kd-tree algorithm

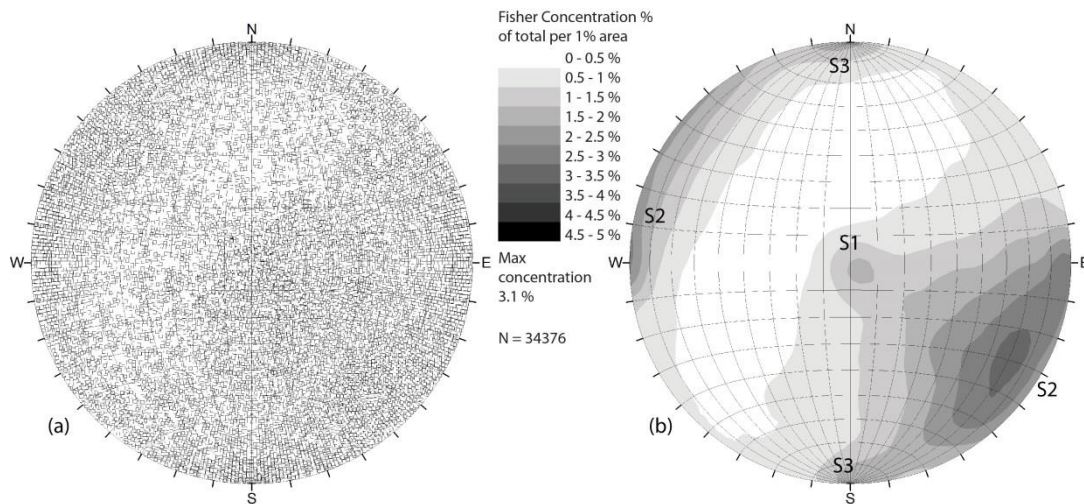
524 The qFacet Kd-tree algorithm was run using the CloudCompare v.2.9 software. The qFacet
 525 Kd-tree is similar to the qFacet FM algorithm. Both divide the point cloud into sub-cells, then
 526 compute elementary planar facets and aggregate them progressively according to a planarity
 527 threshold into polygons. However, the Kd-Tree algorithm recursively subdivides a 3D cloud
 528 into quarter cells until all points within the cell fit a best-fitting plane using the threshold
 529 defined by the root-mean-square of the maximum distance. With this technique, a lattice of
 530 elementary cells of unequal sizes is used to define the discontinuity planes.

531 The parameters used to calculate the cell fusion (maximum angle and maximum relative
 532 distance), the maximum distance of a point to a best-fitting plane, the minimum points per
 533 facet, and the maximum edge length used to extract the facet contour are listed in Table 7 (see
 534 Dewez et al., 2015 for details).

535 Table 7 Parameters used by the qFacet Kd-tree algorithm.

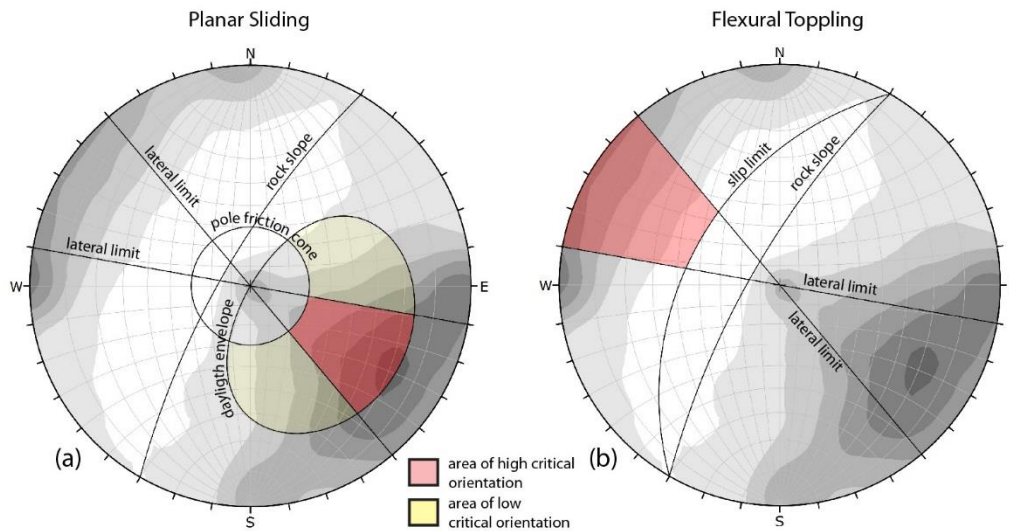
max angle	max relative distance	max distance @ 99%	minimum points per facet	max edge length
10°	1 m	0.1 m	100	0.86 m

536 Using the parameters described in Table 7, the qFacet Kd-tree algorithm detected 34376
 537 discontinuity planes. This is significantly more planes than was detected by the qFacet FM and
 538 DSE algorithms. Again, the planes have a high dispersion in their orientation, and the
 539 maximum pole concentration occurs in the SE quadrant of the stereonet (Fig. 19). Similar to
 540 the previous methods, three principal discontinuity sets can be recognized (Fig. 20b) with the
 541 same general orientations as identified before.



542
 543 Fig. 19 a) stereographic projection (lower hemisphere and equal area) of the poles of the
 544 discontinuities detected by the qFacet Kd-tree algorithm and b) relative contour plot.

545 The calculated number of discontinuity intersections was more than 140,000. Due to this large
 546 number, only the planar sliding and flexural toppling failure modes are considered. A kinematic
 547 analysis suggests that planar sliding could be a critical failure mechanism for 34% of the 34376
 548 detected discontinuities, and these discontinuities essentially occur in set S2. A kinematic
 549 analysis for flexural toppling suggests that only the 8% of the detected discontinuities could be
 550 critical for this mechanism.



551

552 Fig. 20 Kinematic analysis of the possible failure mechanisms involving the discontinuities (a
 553 - planar sliding and b - flexural toppling) formed by the discontinuities detected by the qFacet
 554 Kd-tree algorithm. The critical intersections fall inside the colored areas (equal angle, lower
 555 hemisphere, stereographic projections).

556 4.3 Comparison of manual and semi-automatic detection methods

557 The discontinuities in the study outcrop were identified and measured by both manual and
 558 automatic analysis of the 3D model derived from a digital photogrammetric survey using a
 559 remotely piloted aircraft. A comparison between these methods is based on the overall number
 560 of identified discontinuities and the general discontinuity orientations and lengths.

561 4.3.1 Number of identified discontinuities

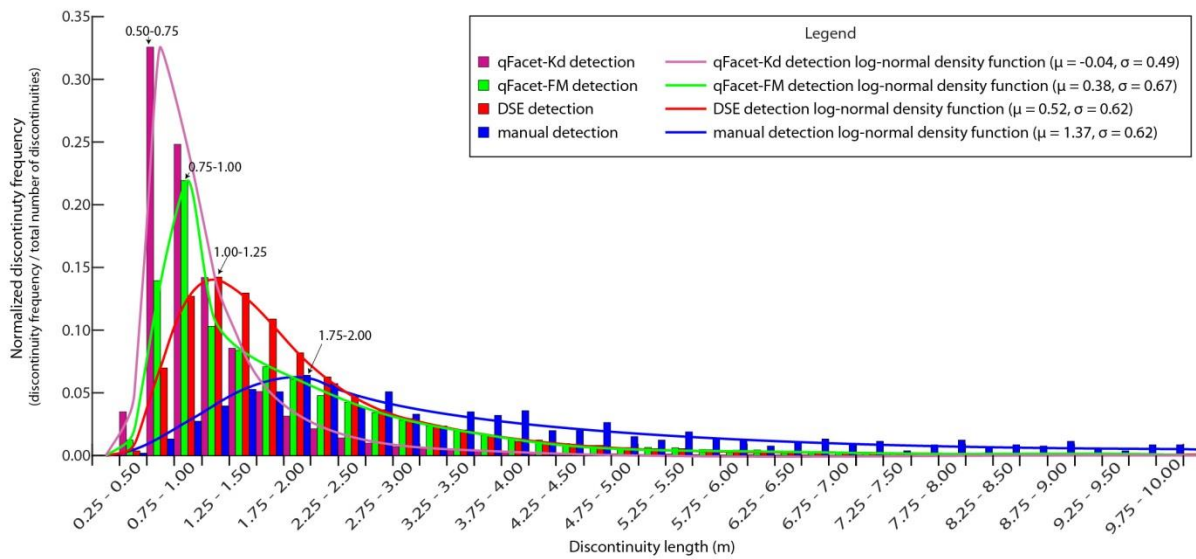
562 A comparison between the manually and automatically detected datasets highlights that the
 563 automatic detection methods recognize roughly 10 to 30 times more discontinuities than the
 564 manual digital mapping method (Table 8). In terms of the automatic identification methods,
 565 the qFacet Kd algorithm, as used in this study, found nearly three times more discontinuities
 566 than the other two methods. The automatic methods for discontinuity detection tend to
 567 subdivide some planes into smaller planes owing to local variations of the surface undulation
 568 and roughness, and thereby identify a larger number of presumed smaller discontinuities.

569 4.3.2 *Discontinuity lengths*

570 A summary of the discontinuity length characteristics obtained from the different methods is
 571 shown in Table 8. The length of discontinuities that were identified using the manual detection
 572 method is greater than the length of the automatically detected discontinuities. The manual
 573 detection method recognized 1036 discontinuities with a mean length of approximately 6 m
 574 (mode ≈ 1.75), whereas the automatic methods, with the parameters used, recognized a larger
 575 number of discontinuities (>10460) with a smaller length (mean length <2.14 m, mode ≈ 0.75
 576 - 1.0) (Table 8; Fig. 21).

577 Table 8. Discontinuity length characteristics obtained with different detection methods
 578 (length in m).

	Manual detection on TDOM	DSE detection	qFacet FM detection	qFacet Kd detection
Number of discontinuities	1036	13185	10460	34276
Mean length of discontinuities	5.96	2.13	1.88	1.11
Median discontinuity length	3.61	1.56	1.33	0.87
Mode of discontinuity length	1.75 - 2.00	1.00 - 1.25	0.75 - 1.00	0.50 - 0.75
Standard deviation of discontinuity length	6.37	2.13	1.62	0.80
Maximum discontinuity length	40.4	42.3	18.3	14.7
Minimum discontinuity length	0.40	0.40	0.36	0.38



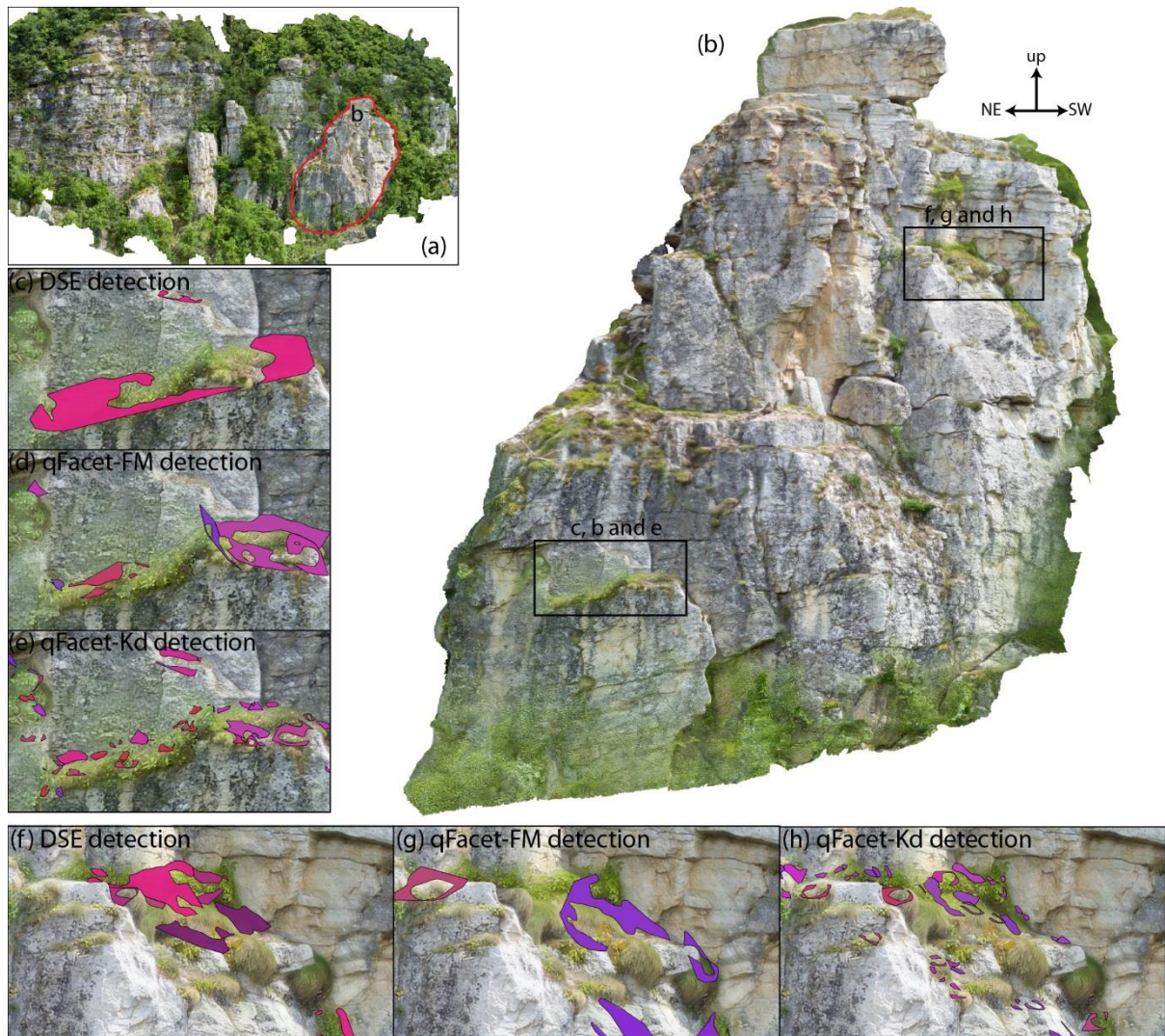
580

581 Fig. 21 Histograms of the discontinuity lengths detected by the different methods (number of
582 bins = 100 for each histogram - solid lines show the log-normal distribution curves.

583 4.3.3 Discontinuity orientations

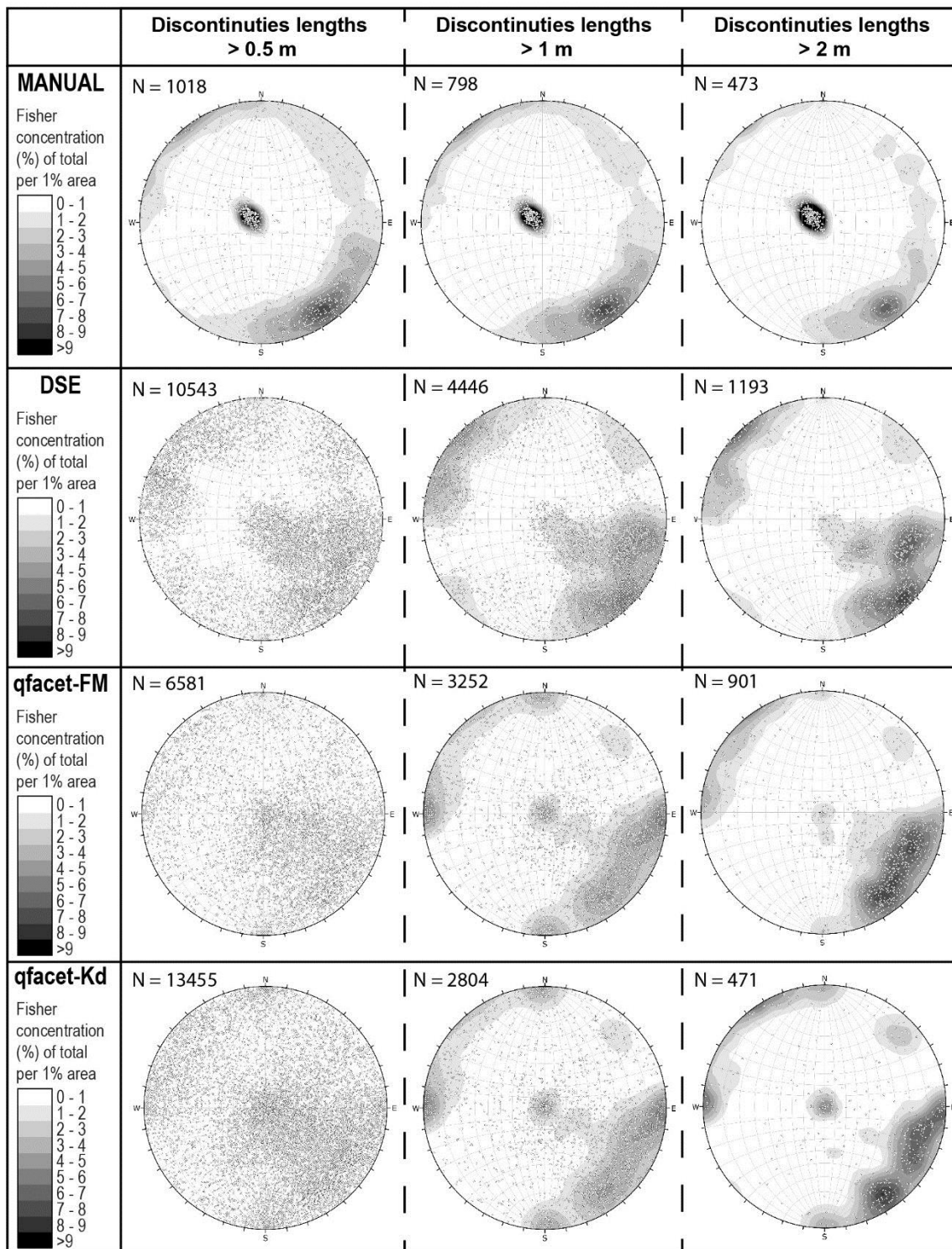
584 The steeper dipping discontinuities identified by manual detection were also found by the semi-
585 automatic detection methods although there are some minor differences in the concentrations
586 of the discontinuity dip directions. The bedding planes that are horizontal to gently dipping are
587 arguably the most dominant discontinuity set in the rock mass. These features were easily
588 identified during manual mapping of the TDOM. However, the automatic discontinuity
589 detection methods do not clearly recognize this set. The bedding often appears only as a trace
590 on the nearly vertical rock faces. The automatic discontinuity detection methods can miss these
591 features even when the bedding trace was large and was the most relevant geomechanical
592 feature in the rock wall. The automatic detection methods can only identify planar facets, and
593 these are often very small along the trace of the bedding and are not detected.

594 The automatic discontinuity detection methods return numerous planes that dip towards the
595 NW that are not visible from the manual inspection of the 3D model. The false detection of
596 some of these discontinuities seems to be associated with the presence of small patches of
597 debris or grassy slopes visible along the wall (Fig. 22). The automatic detection algorithms do
598 not properly discriminate between features that are discontinuities and those that are caused by
599 other features captured in the 3D model.



600
 601 Fig. 22 Images of (a) 3D rock slope model and (b) enlargement of regions showing examples
 602 of the discontinuity planes erroneously detected by the DSE (c)(f), qFacet FM (d)(g) and qFacet
 603 Kd-tree (e)(h) algorithms due to the misinterpretation of small patches of debris and vegetation.

604 To avoid the false detection of discontinuities due to small parts of the outcrop characterized
 605 by debris and natural slope surfaces, and taking into account the differences in the dimensions
 606 of the detected planes, we have considered only the recognized discontinuities that have a
 607 length of more than 0.5, 1 and 2 m (Fig. 23). In fact, the length can be one of the more sensitive
 608 parameters conditioning the semi-automatic recognition of the fractures.



609

610 Fig. 23 Comparison of discontinuity datasets with different length cutoffs, detected by manual
611 and semi-automatic methods. The number of discontinuities with length >2 m are 9%, 9% and
612 1% of the total planes identified by DSE, FM and Kd methods, respectively.

613 The results of this analysis (Fig. 23) indicate that as the cutoff length is increased: a) the number
614 of the planes identified by the manual and automatic methods decreases and approaches a more

615 similar number, b) the dispersion in the fracture orientation considerably decreases, and c) the
616 overall discontinuity orientations resulting from the automatic detection methods used during
617 this study (DSE, qFacet FM, and qFacet Kd) become more similar to each other and do not
618 show any noteworthy differences.

619 Nevertheless, remarkable differences remain between the manual and automatic datasets: a)
620 the numerous automatically detected planes (but not discontinuities) that dip towards the NW
621 are still present, and b) the bedding (i.e., the most dominant discontinuity set) is still not clearly
622 identified by the automatic methods. In any case, the choice to discriminate the detected
623 fractures by their length appears somewhat arbitrary and may not be justifiable *a priori*.

624 4.3.4 *Instability mechanisms inferred from identified discontinuities*

625 The differences in the results from the manual and semi-automatic methods affect the
626 interpretation of possible structurally-controlled failure mechanisms expected in the rock slope.
627 Table 9 shows the percentage of the discontinuity planes and intersections that could be critical
628 for each dataset, for a slope dipping 75° towards 300° and assuming a friction angle of 30° . A
629 lateral instability limit of 20° was also used. In particular, the three datasets based on semi-
630 automatic detection overestimate the planar and wedge sliding mechanisms by a factor of
631 roughly 3 times compared the manual discontinuity mapping. Effectively, a preliminary
632 analysis of the collapse phenomena that have already affected the slope confirms how the
633 toppling (flexural, oblique and direct) is probably the most widespread and dangerous
634 instability mechanism, while the planar and wedge sliding are less frequent. This observation
635 was also supported by the geologists of ARPA Piemonte.

636 Table 9 Comparison of the kinematic analyses for different detection methods for a slope
 637 dipping 75° towards 300°.

Discontinuity detection method	Planar sliding (% of all detected discontinuities)	Flexural toppling	Wedge sliding (% of calculated intersections of all detected discontinuities)	Direct toppling	Oblique toppling
manual	10%	4%	12%	2%	5%
DSE	31%	11%	39%	2%	10%
qFacet FM	33%	7%	34%	2%	5%
qFacet Kd	34%	8%	n/a	n/a	n/a


638

639 5 Conclusions

640 In this work, we presented a workflow for the detection of the discontinuities exposed in a sub-
 641 vertical rock slope using a remotely piloted aircraft system and digital photogrammetry (Fig.
 642 5). This approach is particularly useful in areas where field mapping and terrestrial
 643 photogrammetry or laser scanner surveys cannot be used because the slope is inaccessible,
 644 unsafe, and characterized by a complex geometry with several shadow areas not visible from
 645 the ground. Results based on the use of CloudCompare software to measure the discontinuity
 646 orientation are presented. To evaluate the quality of the discontinuity mapping, we compared
 647 the obtained results with *in situ* manual mapping and with the well-known software 3DM
 648 Analyst©.

649 The proposed procedure results in the generation of a 3D digital model of the rock slope; this
 650 can be referred to as a texturized digital outcrop model (TDOM). This model can be used to
 651 visually recognize and manually map discontinuities in the outcrop. In our case, a planar
 652 stereoscopic mirror device (SD2220W) that allows a stereoscopic view of the model was used.
 653 Mapping the recognized discontinuities was performed by sampling the points in the TDOM
 654 belonging to each discontinuity plane and calculating the 3D best-fit plane by a least-squares-
 655 fit approach. The discontinuity orientations were verified by comparing the manual digital
 656 mapping in the TDOM with the orientation of some control planes measured directly on the
 657 field with a compass-clinometer. The manual digital mapping generated results that are
 658 equivalent to the field measurements because the orientations were within 3° of each other.

659 A comparison of TDOMs generated with and without the use of GCPs shows that the difference
660 in the relative accuracy is small. While the use of ground control points is usually the best
661 solution, it usually takes less effort and is much faster to acquire field data only relying on the
662 GPS coordinates recorded by the UAV. The resulting TDOM created using the digital images
663 and their GPS coordinates may be offset from the real coordinates but its scale and orientation
664 should be relatively accurate.

665 Three different techniques to semi-automatically detect discontinuities in the  were
666 tested (DSE, qFacet FM, and qFacet KD-tree). These techniques identify planes within the
667 point cloud by finding groups of points falling within planar regions. A comparison of the
668 results with the manual analysis shows that the semi-automatic methods tend to recognize
669 roughly 10 to 30 times more discontinuities than the manual digital mapping method. The semi-
670 automatic methods also tend to find smaller discontinuities, due to their tendency to subdivide
671 the actual discontinuities into smaller planes. The automatic methods can erroneously identify
672 planar features that do not represent real discontinuities (e.g., patches of debris or a natural
673 slope).

674 The most important observation is that the automatic methods do not work well for detection
675 of discontinuities that are perpendicular to the slope face such as bedding planes in our case
676 study. Geological structures that are primarily exposed on rock faces as traces, (bedding planes
677 in the case study), are frequently the most relevant structures. The case study showed that the
678 automatic mapping algorithms did not identify many of the bedding planes even when these
679 occur as long trace length features in the 3D model. In contrast, the texture corresponding to
680 these traces, which is provided in the TDOM, along with the experience of the mapper allow
681 manually digital mapping to capture the bedding planes. The difference in detection of
682 discontinuities can adversely influence the kinematic analysis of the rock slope failure
683 mechanisms.

684 While the automatic methods have some limitations, their prime advantage is the large number
685 of features that can be automatically mapped in a relatively short time, which could be
686 important during an emergency operation. However, the obtained results must be accurately
687 checked by manual validation before using them, and this can take a great deal of time.

688 The proposed procedure for discontinuity detection using the RPAS-DP illustrated in Fig. 5
689 takes into account the advantages and limitations of this technique and the algorithms for the
690 automatic detection of discontinuities. The use of the virtual outcrop model obtained from
691 RPAS-DP solves many practical challenges for mapping discontinuities that exist with other
692 techniques. The advantages and limitations of the method are listed in Table 10. With a TDOM,
693 it is possible to repeat discontinuity analysis by different operators and to use different manual
694 and automated techniques. A high-resolution TDOM (<1 cm) allows an accurate manual
695 analysis of a rock slope, especially if the TDOM is examined using a stereoscopic device that
696 gives the mapper a better understanding the rock slope geometry. Nevertheless, it is important
697 to note that field surveys are still important for validating the orientation of the TDOM and for
698 evaluating discontinuities parameters such as aperture, roughness, and infilling.

699 Table 10. Advantages and limitations of RPAS-DP.

Advantages	Limitations
Can accurately map discontinuities by creating a high-resolution TDOM (<1 cm) with results comparable to field measurements	Complex vertical rock slopes could require RPAS with proximity sensors (more expensive RPAS)
Dramatic increase of data because inaccessible or hidden portions of the slope are captured in the model	Possible regulatory restrictions on RPAS flights (e.g., licenses and permits)
Substantial time savings during discontinuity orientation measurements	Wind or critical meteorological conditions can hamper image acquisition using RPAS
Repeatability of measurements by different operators at different times	Time of flight is limited by battery duration which can be critical for investigation of large areas
Safe methodology especially for an unstable rock slope	If the morphology of study area is complex, manual remote control of RPAS can be necessary; this requires good piloting skills

700 Considering the time required to obtain the final results, we found that the automatic mapping
701 procedures are faster than the manual method in the identification of discontinuities. However,
702 taking into account the time needed for effective filtering of vegetation (mandatory for the
703 automatic procedures and not so important for manual), and the validation of results, the
704 difference in time and effort between the manual and automatic mapping becomes small.
705 Manual mapping does depend on the experience of the operator, but the result is a sequence of
706 selected and validated discontinuity measurements. The time that is required to complete the
707 discontinuity mapping is important in particular if the operation is performed in an emergency

708 condition, and the choice of manual or automatic procedure should consider the complexity of
709 the area being mapped.

710 This case study discussed many critical issues when using images collected by a RPAS for the
711 identification of rock wall discontinuities and we hope that this paper can be a useful guide to
712 others using a RPAS for discontinuity measurements.

713 **Acknowledgments**

714 We would like to thank Daniele Bormioli of ARPA Piemonte and Aldo Acquarone for their
715 support in the identification of the Ormea case study.

716 **Funding sources**

717 This research did not receive any specific grant from funding agencies in the public,
718 commercial, or not-for-profit sectors.

719 **References**

- 720 Agisoft Photoscan Professional. Available online: <http://www.agisoft.ru/>
- 721 Bellian, J.A., Kerans, C., Jennette, D.C., 2005. Digital outcrop models: applications of
722 terrestrial scanning lidar technology in stratigraphic modeling. *Journal of Sedimentary*
723 *Research*, 75(2), 166-176.
- 724 Bemis, S.P., Micklethwaite, S., Turner, D., James, M.R., Akciz, S., Thiele, S.T., Bangash,
725 H.A., 2014. Ground-based and UAV-based photogrammetry: A multi-scale, high-
726 resolution mapping tool for structural geology and paleoseismology. *Journal of*
727 *Structural Geology*, 69, 163-178, doi: 10.1016/j.jsg.2014.10.007
- 728 Biber, K., Khan, S.D., Seers, T.D., Sarmiento, S., Lakshmikantha, M.R., 2018. Quantitative
729 characterization of a naturally fractured reservoir analog using a hybrid lidar-gigapixel
730 imaging approach. *Geosphere*, 14(2), 710-730.
- 731 Birch, J.S., 2006. Using 3DM Analyst mine mapping suite for rock face characterization, In
732 F. Tonon and J. Kottenstette (eds.), *Laser and Photogrammetric Methods for Rock Face*
733 *Characterization*, Proc. 41st U.S. Rock Mechanics Symp., Golden.

734 Casella, E., Rovere, A., Pedroncini, A., Stark, C.P., Casella, M., Ferrari, M., Firpo, M., 2016.
735 Drones as tools for monitoring beach topography changes in the Ligurian Sea (NW
736 Mediterranean). *Geo-Marine Letters*, 36(2), 151-163.

737 Cawood, A.J., Bond, C.E., Howell, J.A., Butler, R.W., Totake, Y., 2017. LiDAR, UAV or
738 compass-clinometer? Accuracy, coverage and the effects on structural models. *Journal*
739 *of Structural Geology*, 98, 67-82.

740 Chen, J., Zhu, H., Li, X., 2016. Automatic extraction of discontinuity orientation from rock
741 mass surface 3D point cloud. *Computers and Geosciences*, 95, 18-31.

742 Chesley, J.T., Leier, A.L., White, S., Torres, R., 2017. Using unmanned aerial vehicles and
743 structure-from-motion photogrammetry to characterize sedimentary outcrops: An
744 example from the Morrison Formation, Utah, USA. *Sedimentary Geology*, 354, 1-8.

745 Colomina, I., Molina, P., 2014. Unmanned aerial systems for photogrammetry and remote
746 sensing: A review. *ISPRS Journal of Photogrammetry and Remote Sensing*, 92, 79-97.

747 Dewez, T.J., Girardeau-Montaut, D., Allanic, C., Rohmer, J., 2016. Facets: a CloudCompare
748 plugin to extract geological planes from unstructured 3D point clouds. *International*
749 *Archives of the Photogrammetry, Remote Sensing and Spatial Information Sciences*,
750 41.

751 Gigli, G., Casagli, N., 2011. Semi-automatic extraction of rock mass structural data from high
752 resolution LIDAR point clouds. *International Journal of Rock Mechanics and Mining*
753 *Sciences*, 48(2), 187-198.

754 Giordan, D., Hayakawa, Y., Nex, F., Remondino, F., Tarolli, P., 2017. The use of remotely
755 piloted aircraft systems (RPAS) for natural hazards monitoring and management,
756 *Natural Hazards Earth System Sciences Discussion*, [https://doi.org/10.5194/nhess-2017-](https://doi.org/10.5194/nhess-2017-339)
757 339.

758 Giordan, D., Manconi, A., Tannant, D.D., Allasia, P., 2015. UAV: Low-cost remote sensing
759 for high-resolution investigation of landslides. In *Geoscience and Remote Sensing*
760 *Symp. (IGARSS)*, IEEE, 5344-5347.

761 Gomes, R.K., de Oliveira, L.P., Gonzaga, L., Tognoli, F.M., Veronez, M.R., de Souza, M.K.,
762 2016. An algorithm for automatic detection and orientation estimation of planar
763 structures in LiDAR-scanned outcrops. *Computers and Geosciences*, 90, 170-178.

764 Gonçalves, J.A., Henriques, R., 2015. UAV photogrammetry for topographic monitoring of
765 coastal areas. *ISPRS Journal of Photogrammetry and Remote Sensing*, 104, 101-111.

766 Goodman, R.E., 1980. *Introduction to Rock Mechanics (Chapter 8)*, Toronto: John Wiley, pp
767 254-287.

768 Guo, J., Liu, S., Zhang, P., Wu, L., Zhou, W., Yu, Y., 2017. Towards semi-automatic rock
769 mass discontinuity orientation and set analysis from 3D point clouds. *Computers and*
770 *Geosciences*, 103, 164-172.

771 Hudson, J.A., Harrison, J.P., 1997. *Engineering Rock Mechanics – An Introduction to the*
772 *Principles*, Pergamon Press.

773 Humair, F., Pedrazzini, A., Epard, J.L., Froese, C.R., Jaboyedoff, M., 2013. Structural
774 characterization of turtle mountain anticline (Alberta, Canada) and impact on rock slope
775 failure. *Tectonophysics* 605, 133–148, doi:10.1016/j.tecto.2013.04.029

776 Jaboyedoff, M., Metzger, R., Oppikofer, T., Couture, R., Derron, M.H., Locat, J., Turmel, D.,
777 2007. New insight techniques to analyze rock-slope relief using DEM and 3D-imaging
778 cloud points: COLTOP-3D software. In *Rock mechanics: Meeting Society’s Challenges*
779 *and Demands (Vol. 1, pp. 61-68)*.

780 Jaboyedoff, M., Oppikofer, T., Abellán, A., Derron, M.H., Loye, A., Metzger, R., Pedrazzini,
781 A., 2012. Use of LIDAR in landslide investigations: a review. *Natural Hazards*, 61(1),
782 5-28.

783 Jordá Bordehore, L., Riquelme, A., Cano, M., Tomás, R., 2017. Comparing manual and
784 remote sensing field discontinuity collection used in kinematic stability assessment of
785 failed rock slopes. *International Journal of Rock Mechanics & Mining Sciences* 97, 24–
786 32.

787 Lucieer, A., Jong, S.M.D., Turner, D., 2013. Mapping landslide displacements using
788 Structure from Motion (SfM) and image correlation of multi-temporal UAV
789 photography. *Progress in Physical Geography*, 38(1), 97-116.

790 Nex, F., Remondino, F., 2014. UAV for 3D mapping applications: a review. *Applied*
791 *Geomatics*, 6(1), 1-15.

792 Niethammer, U., James, M.R., Rothmund, S., Travelletti, J., Joswig, M., 2012. UAV-based
793 remote sensing of the Super-Sauze landslide: Evaluation and results. *Engineering*
794 *Geology*, 128, 2-11.

795 Powers, P.S., Chiarle, M., Savage, W.Z., 1996. A digital photogrammetric method for
796 measuring horizontal surficial movements on the Slumgullion earthflow, Hinsdale
797 County, Colorado. *Computers and Geosciences*, 22(6), 651-663.

798 Pringle, J.K., Westerman, A.R., Clark, J.D., Drinkwater, N.J., Gardiner, A.R., 2004. 3D high-
799 resolution digital models of outcrop analogue study sites to constrain reservoir model
800 uncertainty: an example from Alport Castles, Derbyshire, UK. *Petroleum Geoscience*,
801 10(4), 343-352.

802 Remondino, F., El-Hakim, S., 2006. Image-based 3D modelling: a review. *The*
803 *Photogrammetric Record*, 21(115), 269-291.

804 Riquelme, A.J., Abellán, A., Tomás, R., Jaboyedoff, M., 2014. A new approach for semi-
805 automatic rock mass joints recognition from 3D point clouds. *Computers and*
806 *Geosciences*, 68, 38-52.

807 Salvini, R., Mastrorocco, G., Seddaiu, M., Rossi, D., Vanneschi, C., 2016. The use of an
808 unmanned aerial vehicle for fracture mapping within a marble quarry (Carrara, Italy):
809 photogrammetry and discrete fracture network modelling. *Geomatics, Natural Hazards*
810 *and Risk*, 1-19.

811 Seers, T.D., Hodgetts, D., 2016. Extraction of three-dimensional fracture trace maps from
812 calibrated image sequences. *Geosphere*, 12 (4): 1323–1340.

813 Slob, S., Hack, R., Van Knapen, B., Kemeny, J., 2004. Automated identification and
814 characterization of discontinuity sets in outcropping rock masses using 3D terrestrial
815 laser scan survey techniques. In *Proc. of the ISRM Regional Symp. EUROCK Eurock*
816 (pp. 439-443).

817 Spreafico, M.C., Francioni, M., Cervi, F., Stead, D., Bitelli, G., Ghirotti, M., Girelli, V.A.,
818 Lucente, C.C., Tini, M.A., Borgatti, L., 2016. Back Analysis of the 2014 San Leo
819 landslide using combined terrestrial laser scanning and 3D distinct element modelling.
820 *Rock Mechanics and Rock Engineering*, 49(6), 2235-2251, doi:10.1007/s00603-015-
821 0763-5

822 Sturzenegger, M., Stead, D., 2009. Close-range terrestrial digital photogrammetry and
823 terrestrial laser scanning for discontinuity characterization on rock cuts. *Engineering*
824 *Geology*, 106, 163–182, doi: 10.1016/j.enggeo.2009.03.004

825 Tannant, D.D., 2015. Review of photogrammetry-based techniques for characterization and
826 hazard assessment of rock faces. *Int. Journal of Geohazards and Environment*, 1(2), 76-
827 87.

828 Tannant, D.D., Giordan, D., Morgenroth, J., 2017. Characterization and analysis of a
829 translational rockslide on a stepped-planar slip surface. *Engineering Geology*, 220, 144-
830 151.

831 Tavani, S., Corradetti, A., Billi, A., 2016. High precision analysis of an embryonic
832 extensional fault-related fold using 3D orthorectified virtual outcrops: The viewpoint
833 importance in structural geology. *Journal of Structural Geology*, 86, 200-210, doi:
834 10.1016/j.jsg.2016.03.009

- 835 Török, Á., Barsi, Á., Bögöly, G., Lovas, T., Somogyi, Á., Görög, P., 2017. Slope stability
836 and rock fall hazard assessment of volcanic tuffs using RPAS and TLS with 2D FEM
837 slope modelling.
- 838 Turner, D., Lucieer, A., Wallace, L., 2014. Direct georeferencing of ultrahigh-resolution
839 UAV imagery. *IEEE Transactions on Geoscience and Remote Sensing*, 52(5), 2738-
840 2745.
- 841 Vöge, M., Lato, M.J., Diederichs, M.S., 2013. Automated rockmass discontinuity mapping
842 from 3-dimensional surface data. *Engineering Geology*, 164, 155-162.
- 843 Westoby, M.J., Brasington, J., Glasser, N.F., Hambrey, M.J., Reynolds, J.M., 2012.
844 'Structure-from-Motion' photogrammetry: A low-cost, effective tool for geoscience
845 applications. *Geomorphology*, 179, 300-314.
- 846 Xu, X., Aiken, C.L., Bhattacharya, J.P., Corbeanu, R.M., Nielsen, K.C., McMechan, G.A.,
847 Abdelsalam, M.G., 2000. Creating virtual 3-D outcrop. *The Leading Edge*, 19(2), 197-
848 202.